

**Mechanically controllable break  
junction  
in liquid environment:  
a tool to measure  
electronic transport through  
single molecules**

INAUGURALDISSERTATION

zur

Erlangung der Würde eines Doktors der Philosophie  
vorgelegt der  
Philosophisch-Naturwissenschaftlichen Fakultät  
der Universität Basel

von

Lucia Grüter

aus Ruswil (LU)

Basel, Juli 2005

Genehmigt von der Philosophisch-Naturwissenschaftlichen Fakultät auf  
Antrag der Herren Professoren:

Prof. Dr. C. Schönenberger  
Prof. Dr. M. Mayor

und der Frau Professorin:

Prof. Dr. E. Scheer

Basel, 1. Juli 2005

Prof. Dr. H.-J. Wirz, Dekan

# Contents

<b>1</b>	<b>Nanogaps fabricated by electrochemical methods</b>	<b>5</b>
1.1	Electrochemical template synthesis of nanowires . . . . .	5
1.1.1	Fabrication of electrochemical wires . . . . .	5
1.1.2	Experimental Results . . . . .	9
1.1.3	Localization and contacting of the nanowires . . . . .	10
1.1.4	Discussion and Conclusion . . . . .	11
1.2	Combination of lithography and electrodeposition . . . . .	11
1.2.1	Structure fabrication . . . . .	12
1.2.2	Experimental Results . . . . .	12
1.3	Discussion and Conclusion . . . . .	15
<b>2</b>	<b>The principle of metallic atomic contacts</b>	<b>17</b>
2.1	Brief history of atomic-sized conductors . . . . .	17
2.2	Principle and fabrication of atomic sized contacts . . . . .	18
2.2.1	Scanning tunneling microscope (STM) . . . . .	18
2.2.2	Mechanically controllable break junction (MCBJ) . . . . .	19
2.3	The conductance of atomic sized metallic contacts . . . . .	26
2.3.1	Conductance steps . . . . .	26
2.3.2	Conductance histograms . . . . .	29
2.3.3	Conductance of a single atom . . . . .	30
<b>3</b>	<b>Sample preparation and description of the setup</b>	<b>33</b>
3.1	Substrate preparation . . . . .	33
3.2	Lithography and metal deposition . . . . .	34
3.2.1	Principle . . . . .	34
3.2.2	Optical lithography . . . . .	34
3.2.3	Electron beam lithography . . . . .	34
3.2.4	Metal deposition . . . . .	35
3.3	Plasma etching . . . . .	35
3.4	The setup . . . . .	36
<b>4</b>	<b>Measurements of atomic contacts in liquid environment</b>	<b>39</b>
4.1	Introduction . . . . .	39
4.2	High conductance regime . . . . .	39

---

4.3	Tunneling regime . . . . .	40
4.3.1	Tunneling through alkanes and alkanethiols . . . . .	44
4.4	Conclusion . . . . .	47
<b>5</b>	<b>Resonant tunneling through a C<sub>60</sub> molecular junction in liquid environment</b>	<b>49</b>
5.1	Introduction . . . . .	49
5.2	Experimental part and measurements . . . . .	51
5.3	Discussion . . . . .	53
5.4	Conclusion . . . . .	60
<b>6</b>	<b>Transport measurements through TTF derivatives in liquid environment</b>	<b>61</b>
6.1	Introduction . . . . .	61
6.2	Electrochemical gating . . . . .	62
6.3	Experimental part and measurements . . . . .	64
6.4	Discussion . . . . .	66
6.5	Conclusion . . . . .	70
<b>A</b>	<b>Experimental details to the C<sub>60</sub> measurements</b>	<b>77</b>
A.1	Measurements of C <sub>60</sub> in DMSO . . . . .	77
A.2	Measurements of C <sub>60</sub> in toluene . . . . .	80
<b>B</b>	<b>Experimental details to the chemistry of the thiols</b>	<b>83</b>
<b>C</b>	<b>Additional data to the TTF measurements</b>	<b>85</b>

# Introduction

Since the discovery of the transistor in 1948 [1] the size of the components in integrated circuits (IC) has been shrinking continuously. The electronic industry has constantly improved the IC fabrication in terms of performance and cost reduction. The speed and performance increase of IC chips are based on the minimum printable feature size. The rate of progress is described by Moore's law which states that the number of transistors per square centimeter roughly doubles every two years.

Meanwhile microelectronics became nanoelectronics, where quantum effects start to play a role. Quantum dots ("artificial atoms"), single electron transistors and resonant tunneling devices (RTDs) have been proposed, fabricated and experimentally explored. In this context hard, rigid molecules (carbon nanotubes) and soft, organic molecules came into play demonstrating the ultimate miniaturization of logic circuits. The use of molecules as building blocks in the construction of electronic circuits is the subject of Molecular Electronics. Besides their main benefit of being small, molecules offer additional advantages such as a cheap production, ability to self-assemble on a surface and additionally their structure is systematically designable.

The first effort in the field of molecular electronics began with the theoretical work of Aviram and Ratner in the 1970s [2]. They proposed that a donor-acceptor compound could act as a molecular rectifier. In the meantime technological advances made it possible to address and investigate a few or even single molecules. The conductance of single molecules has been addressed in several experiments where quantum phenomena such as Coulomb blockade and Kondo effect [3, 4], negative differential resistance [5] and logic gates [6] were pointed out. Different techniques have been used to address single or a few molecules. Fixed contact arrangements such as nanopore systems [7], nanogaps fabricated by shadow evaporation [8], electromigration [4] or electrochemical methods [9] have been realized. Alternatively, scanning tunneling microscope (STM) [10, 11, 12] and break junction techniques [7, 13, 14, 15] offer a tunable gap between the two electrodes to characterize molecules. Break junctions offer an additional mechanical stability compared to the STM. But the implementation of a third electrode which is needed to tune the conductance of the molecule, remains delicate although recent work shows it can be done [16].

That an electrolyte can provide an excellent gate efficiency has been demonstrated on carbon nanotube field-effect transistors [17] and recently this effect has been studied for organic molecules using a STM [18, 19]. Additionally a chemical environment allows *in situ* electrochemistry experiments.

Although a remarkable progress occurred in the last years many challenges in molecular electronics remain. The main problem is the lack of reproducibility and control over the molecule-metal interface [20, 21]. The mobility of metal atoms of the electrodes leads to instability of the interface and affects the conductance properties of the device. Also the process of self-assembly can affect the morphology of the metal surface [22]. Several important factors in molecular transport (e.g. the exact geometry of the molecule in the junction) still have to be understood.

The concept of molecular electronics demonstrates not only to be an interesting research area but it also offers a high potential for the future electronics. Large scale molecular devices have been developed and are partially already in application (organic light emitting diodes, liquid crystal displays, organic displays). But whether single molecules will ever be used in electronics is still an open question. Carbon nanotubes are attractive candidates for many applications (sensors, data processing, field emitter [20]) but also there is still a long way to go.

## This thesis

This thesis discusses electronic transport measurements of single molecules in a liquid environment with the ultimate goal of demonstrating a molecular transistor addressed by a liquid gate. A mechanical controllable break junction with an integrated liquid cell is used as the measurement tool. We first studied the influence of different solvents on the conductance of gold junctions in the regime of tunneling and true metallic contacts. These measurements served as control experiment for the electrical characterization of single molecules. We then measured the conductance traces of thiolated  $C_{60}$  molecules while varying the electrode separation. The shape of the curves was found to be strongly influenced by the solvent. By using a resonant tunneling model, the electronic tunneling rates could be extracted. Finally, the effect of a liquid gate was tested on several tetrathiafulvalene (TTF) compounds. This thesis is organized in the following way.

- The first chapter presents two different approaches for producing nanogaps in order to contact single molecules. One is based on electrochemical wires grown in pores, whereas the other method concerns the electrochemical narrowing of lithographically defined gaps.
- The second chapter introduces the break junction and gives a short overview over its research field. Discussed are the geometry and the mechanical properties of the break junction and finally the conductance of atomic contacts.
- Chapter 3 is dedicated to the fabrication of break junction samples and the measurement setup.
- Electric conductance measurements of atomic contacts in liquid environments are presented in the fourth chapter. This work was done with the perspective of measuring single molecules in the break junction. Also discussed is tunneling through alkanethiols.
- Chapter 5 presents electric transport measurements through thiolated  $C_{60}$  molecules in a liquid environment. When varying the electrode separation a peak in the conductance traces has been observed. By applying a resonant tunneling model, we were able to extract electronic tunneling rates.
- In Chapter six transport measurements through tetrathiafulvalene (TTF)-based molecules with an electrochemical gate are shown. A possible gate effect is discussed based on the  $I$ - $V$  characteristics.





# Chapter 1

## Nanogaps fabricated by electrochemical methods

In the first year of my Ph.D. work the fabrication of nanosized gaps based on electrochemistry was tested. Two methods are described and discussed in this chapter. The first method is the growth of multilayered electrochemical wires. A subsequent etching of the middle layer results in a gap in the nanometer range. The second method is based on lithographically fabricated gaps with a reduction of the gap size by electrochemical deposition from an ionic metal solution or by an etching and deposition technique in HCl or water.

### 1.1 Electrochemical template synthesis of nanowires

Electrochemically synthesized nanowires are obtained by filling a porous polycarbonate membrane (template) that contains a large number of straight cylindrical holes [23, 24]. A metal layer is evaporated on one side of the membrane. Fig. 1.1 shows a schematics of the membrane fixed in an electrochemical cell which is filled with a metal ion solution. By applying a constant voltage between the membrane (working electrode) and the counter electrode, the metal ions are deposited from the solution into the pores of the membrane. The current is measured during the deposition with a potentiostat. We deposited a thin layer of a second metal in the center of the pore, as shown in Fig. 1.1. After dissolving of the membrane, a specific etching of the middle layer leads to a gap with a size in the nanometer range.

#### 1.1.1 Fabrication of electrochemical wires

The pores of the track etched polycarbonate membrane (PCTE from Osmonics) have a diameter of 20 nm and a length of 6  $\mu\text{m}$ . A 50 nm thick gold layer, serving as working electrode, is evaporated on one side

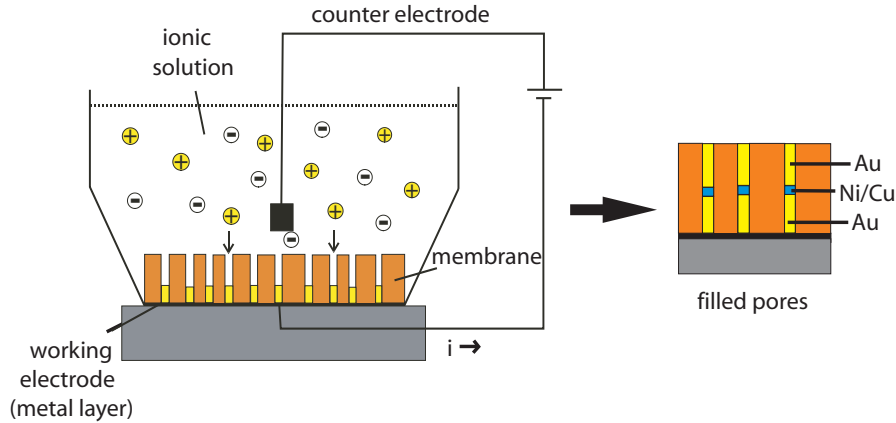


Figure 1.1: Schematics of electrochemical template synthesis of nanowires in a porous membrane. An evaporated gold layer on one side of the membrane serves as working electrode. At a certain voltage between the working electrode and the counter electrode, the metal cations are reduced at the working electrode and deposited in the pores, forming a metal wire. The pores are filled with layers of two different metals.

of the membrane. The membrane is then fixed in the electrochemical cell made of teflon with the gold layer facing down onto a conducting substrate. The schematics of the electrochemical cell is given in Fig. 1.2. A voltage is applied between the working electrode and the counter electrode, separated by an ionic solution. The potentiostat controls the potential between the working electrode and the reference electrode. The reference electrode (saturated calomel electrode, SCE) is kept at a fixed reference potential. The current measured by the potentiostat flows between the working electrode and the counter electrode, but there is no current flowing through the reference electrode, which is used to measure the potential.

The electric field at the surface of the electrodes leads to an electron transfer between the electrode and the ions or molecules in the solution near the electrode surface. Reduction and oxidation processes take place. In the discussed experiment metal cations are reduced ( $\text{Au}^{+1} \rightarrow \text{Au}$ ,  $\text{Ni}^{+2} \rightarrow \text{Ni}$ ,  $\text{Cu}^{+2} \rightarrow \text{Cu}$ ) at the working electrode and deposited in the pores of the membrane. We focus on the electroplating of gold, nickel and copper. Electroplating is a process in which metal ions react at a cathode to form elemental metals.

The following aqueous electrolytes have been used: gold solution: 0.05 M sodium gold sulfite ( $\text{Na}_3\text{Au}(\text{SO}_3)_2$ ); nickel solution: 0.4 M  $\text{NiSO}_4 \cdot 6\text{H}_2\text{O}$  + 45 g (0.32 mol)  $\text{H}_3\text{BO}_3$  per liter solution (pH=3.6) used as 1:10 dilu-

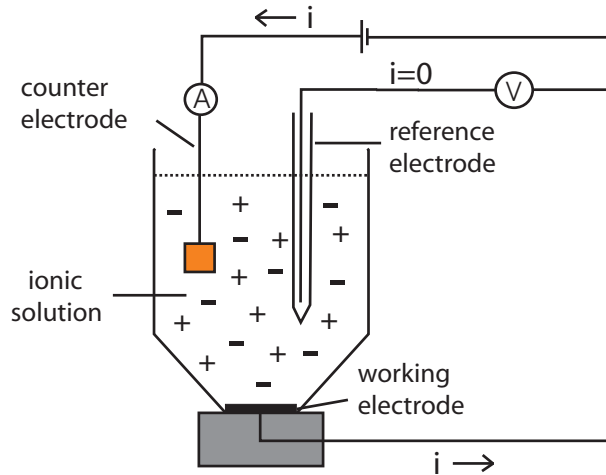


Figure 1.2: Electrochemical cell with a three-electrodes configuration for the fabrication of electrochemical wires.

tion; copper solution: 37.0 mM solution of  $\text{CuSO}_4 \cdot 5\text{H}_2\text{O}$ , 10 g/l Sodium citrate and 2 g/l NaCl. The applied voltages were -0.8, -0.9 and -0.1 V for Au, Ni and Co, respectively.

The detailed fabrication of multilayered wires is the following:

1. Mounting of the membrane into the electrochemical cell and immersion into deionized water for some minutes (wetting of the pores).
2. Filling of the cell with the Au solution. Deposition of Au for 3500 s at -0.8 V at constant stirring, the deposition rate is about 0.7 nm/s. The pores are now filled to  $\sim 50\%$  with deposited Au. After this step, the teflon cell has to be rinsed with deionized water.
3. Filling of the electrochemical cell with the nickel solution and using ultrasonic agitation for two minutes. During the deposition, the growth speed is about 1.5 nm/s at -0.9 V. The cell has to be rinsed properly after the deposition.
4. Again filling the electrochemical cell with the Au solution and using ultrasonic agitation for two minutes without applying a voltage. Thereafter Au is deposited at -0.8 V under constant stirring until the pore is filled up.

An alternative is to deposit copper instead of nickel in the intermediate step. Copper turned out to grow more homogeneously than nickel.

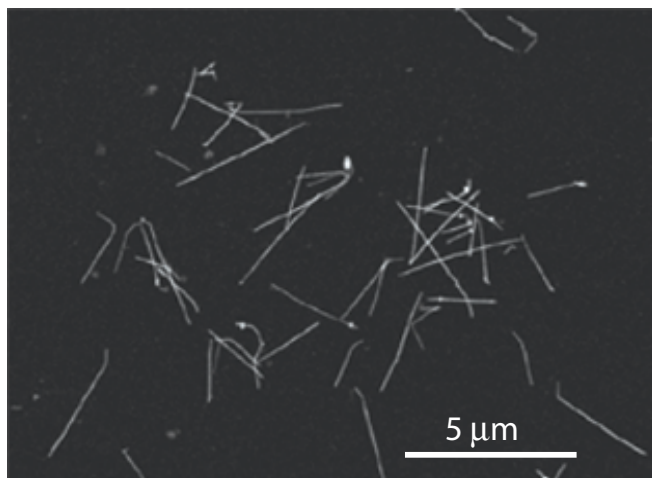


Figure 1.3: SEM picture of gold wires on a silicon substrate, obtained by electrochemical template synthesis.

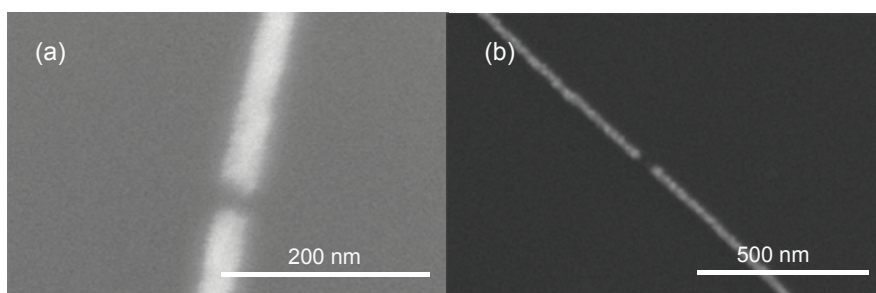


Figure 1.4: Electrochemical gold wires after etching off the nickel. Deposition time for nickel was for both wires 33 s at  $V = -0.9$  V but the resulting gaps have different sizes, in (a)  $\sim 25$  nm and in (b)  $\sim 60$  nm.

After electroplating, the gold electrode on the membrane was removed with an acetone saturated cue-tip by scraping off gently. The membrane was then cut in small pieces and put on a silicon sample with lithographically defined contact pads and small crosses for the orientation. The sample was immersed in dichloromethane ( $\text{CH}_2\text{Cl}_2$ ) at  $40^\circ\text{C}$  for 10 minutes to dissolve the membrane and subsequently rinsed in chloroform and ethanol. The wires were then randomly spread over the sample surface. Fig. 1.3 shows a SEM picture of obtained gold wires on a silicon substrate.

The next step was to selectively etch off the metal layer (Cu or Ni)

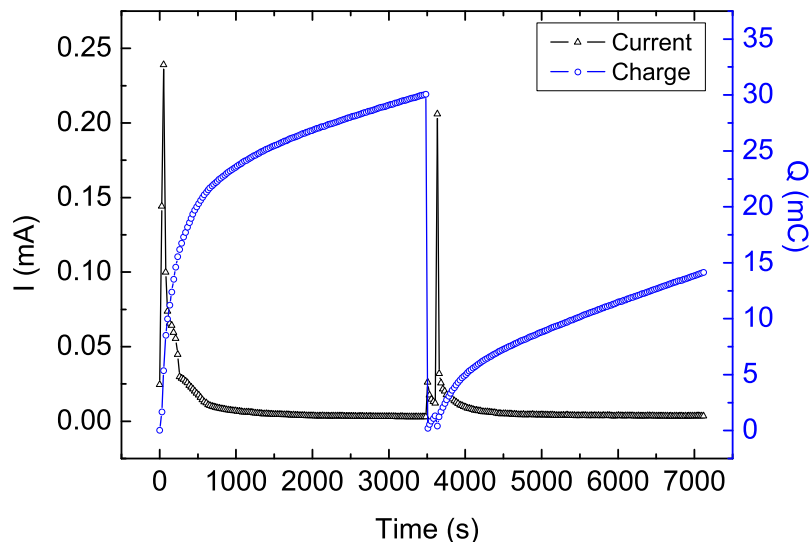


Figure 1.5: Alternating deposition of gold, nickel and gold. Measured current and charge during the deposition of Au/Ni/Au. The total deposition time was 7000 s.

between the gold layers, in order to get two half wires with a very small separation in between, see Fig. 1.4. For the nickel etchant,  $\text{H}_2\text{SO}_4$  at 98% concentration and  $\text{H}_3\text{PO}_4$  at a 42% concentration were mixed in the ratio 1:6. The etching time was 8 minutes, afterwards the sample was rinsed in deionized water. The copper etchant consisted of an aqueous solution of 25 ml/l  $\text{H}_2\text{SO}_4$  at 98%, 175 ml/l  $\text{H}_2\text{O}_2$  at 30% and few drops of  $\text{H}_3\text{PO}_4$  at 85%. An etching time of 7 minutes was needed to remove the copper layer. Afterwards the sample was rinsed in deionized water.

### 1.1.2 Experimental Results

During the electrodeposition, a constant voltage is applied across the membrane. We recorded the electrical current  $I$  and the deposited charge ( $Q$ ) versus time  $t$  for the reduction of  $\text{Au}^{1+}$ ,  $\text{Ni}^{2+}$  and  $\text{Cu}^{2+}$ . A typical  $I/t$  and  $Q/t$  curve for the deposition of Au/Ni/Au wires is shown in Fig. 1.5. First, gold was deposited during 3500 s, the total measured charge continuously increased and reached 30 mC. The current was always large at the beginning of the deposition, but reduced within 700-1000 s to a constant value of several  $\mu\text{A}$  (here at around 3  $\mu\text{A}$ ). This observation is attributed to mass transport limitations of the ions. At the electrode region the ionic concentration gets partially

depleted resulting in a reduction of the current. The same behaviour could be observed for the second gold layer, the deposited charge added up to 14 mC. The intermediate nickel layer was grown for 133 s at an averaged growth speed of 1.5 nm/s. 1.5 mC were deposited in this time. After a sharp increase, the current decreased again during the first 20 s and stayed constant at a value of  $\sim 10 \mu\text{A}$ .

Imaging of the wires with SEM showed a big variety of gap sizes. This reveals an inhomogeneous nucleation of the nickel layer after the first gold deposition resulting in a big variety of nickel thicknesses and gap sizes. An example for this is shown in Fig. 1.4. For both wires, the Ni deposition time was 33 s, but the resulting gap size is in (a) 25 nm and in (b) 60 nm. The nominal thickness deduced from the averaged growth speed of 1.5 nm/s should be 50 nm. We tried to overcome this problem by using ultrasonic agitation before applying the voltage. However, there was no substantial improvement. Also the second gold layer seemed to grow not as homogenous as the first layer, therefore we got different lengths of wires. But this was of less importance, as they were still long enough to be contacted by electron beam lithography (an example is shown in Fig. 1.6).

### 1.1.3 Localization and contacting of the nanowires

The imaging and localization of the wires was done with the SEM. Wires (longer  $3 \mu\text{m}$ ) with gaps are localized with help of markers in the shape of small crosses. These crosses are fabricated in the first electron beam lithography step on the silicon substrate (before the wire deposition) and are distributed equally spaced between the contact pads. The contacts to the wires were carried out in a second electron beam lithography step

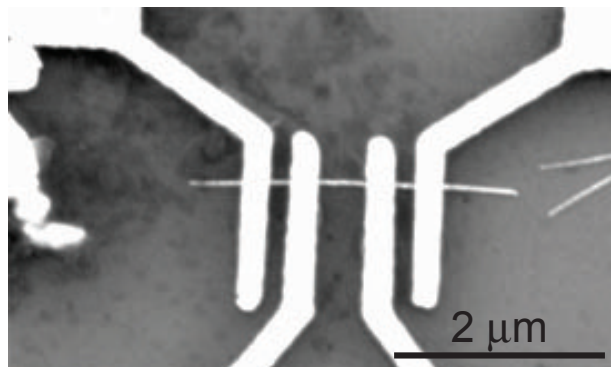


Figure 1.6: Electrochemically grown nanowire with four Au contacts for a 4-point measurement.

consisting of four lines across the electrochemical wire, see Fig. 1.6. The lines were linked to the contact pads.

#### 1.1.4 Discussion and Conclusion

Nanogaps could be produced by using electrochemically grown nanowires with gaps of sizes between 20-100 nm. The problem of this method was the low yield of wires with gaps. A possible reason could be that they broke during the chemical treatment. Another drawback was the inhomogeneous nucleation and growth of the metal in between the two gold layers and also of the second gold layer. This leads to a large variety of gap sizes. A further disadvantage was the large number of processing steps which in addition lowered the yield. Also, the searching and imaging of the wires with small gaps was very time consuming.

## 1.2 Combination of lithography and electrodeposition

The second technique to fabricate nanogaps is referred as “electrochemical narrowing” and combines electron beam lithography and electrochemistry. Two electrodes with a small separation are made by lithography. Afterwards, a droplet of a low concentrated HCl is put on the gap and a bias voltage is applied between the two electrodes. Metal ions are etched off uniformly from the anode, guided by the electric field and deposited on the cathode. This leads to a tip formation on one side and, consequently, the gap decreases and finally closes. An external resistor is used, which is connected in series to one of the electrodes. According to Tao *et al.* [9], the external resistance is controlling the gap size and leads to a self-termination mechanism. The effective voltage for etching and deposition is given by

$$V_{gap} = \frac{R_{gap}}{R_{gap} + R_{ext}} V_0 \quad (1.1)$$

where  $R_{gap}$  is the resistance between the two electrodes,  $R_{ext}$  the external resistance and  $V_0$  the total applied bias voltage. At the beginning of the process, when the gap is still large,  $R_{gap} \gg R_{ext}$  and  $V_{gap} \sim V_0$ , the entire applied voltage drops over the gap and is used for etching and deposition. While the size of the gap gets narrow, the etching and deposition rates are slowed down. The processes at the electrodes terminate when  $R_{gap} \ll R_{ext}$  and consequently  $V_{gap} \sim 0$ .

The experiment was carried out not only with HCl but also with an ionic metal solution and with deionized water.

### 1.2.1 Structure fabrication

The first step was the fabrication of the structure by lithography. It included two contact pads and a pair of electrodes with a separation between 50-300 nm. The two electrodes were in contact with the two pads, see Fig. 1.7.

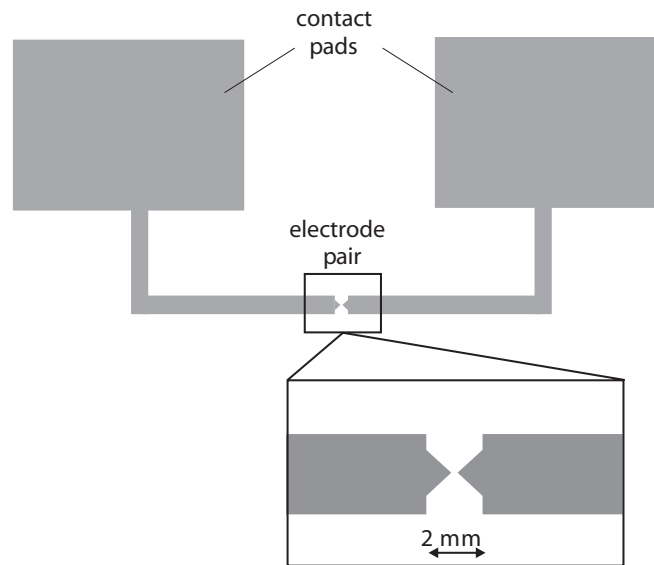


Figure 1.7: Schematics of an lithography structure used for electrodeposition. The separation between the two electrode tips is 50-300 nm.

### 1.2.2 Experimental Results

The external resistor was varied between 1 k $\Omega$  and 1 M $\Omega$ . The contact to the structure was provided by two needles. A micropipette was used to put a droplet of solution on the region between the two electrodes. We tested several solutions for etching and deposition. The voltage was applied between the two electrodes. There was no counter electrode or reference electrode involved in the experiment.

- Gold solution: We used a 0.05 M sodium gold sulfite ( $\text{Na}_3\text{Au}(\text{SO}_3)_2$ ) bath from Metakem. The applied potential was varied between -0.8 V and -1.0 V. The gold deposition on one electrode was large, but there was no etching observable on the other electrode. Consequently, one electrode became wide and high, as the growth occurred not only horizontally but also vertically. An example is shown in Fig. 1.8 where (a) represents an electrode pair before



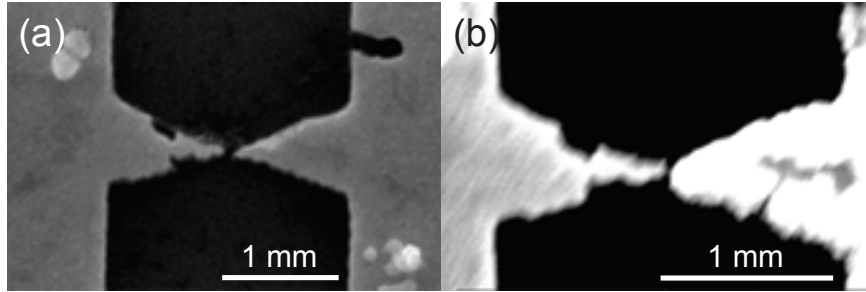


Figure 1.8: Electrode pair (a) before gold deposition and (b) after 7 minutes of gold deposition at  $-0.88\text{ V}$ ,  $R_{ext}=220\text{ k}\Omega$ , in a droplet of gold sulfite solution placed on top of the electrodes.

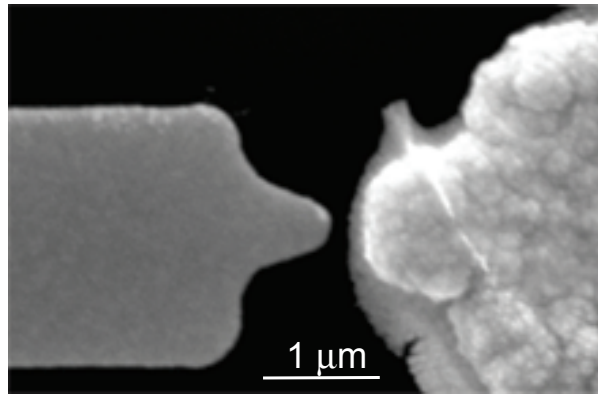


Figure 1.9: SEM picture after 10 minutes of gold deposition (from  $(\text{Na}_3\text{Au}(\text{SO}_3)_2)$  solution) at  $-1.0\text{ V}$  with an external resistor of  $220\text{ k}\Omega$ . Remarkable is the unwanted horizontal and vertical growth of gold. There is no etching at the left electrode.

adding the gold solution and (b) after gold deposition at  $-0.88\text{ V}$  for 7 minutes with  $R_{ext}=220\text{ k}\Omega$ .

The SEM picture in Fig. 1.9 shows an even more impressive example of gold growth in lateral and vertical direction after 10 minutes of gold deposition at  $-1.00\text{ V}$  with  $R_{ext}=220\text{ k}\Omega$ .

- HCl solution: The following concentrations of HCl were tested: 100 mM, 10 mM, 5 mM, 1 mM and 0.5 mM. The voltage was varied between  $-0.5\text{ V}$  and  $-1.4\text{ V}$ . In contrast to the gold solution, the etching of one electrode was very strong with HCl. However, the

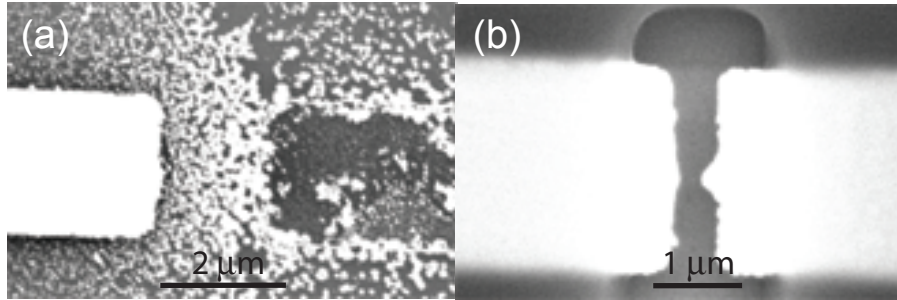


Figure 1.10: (a) SEM picture of an electrode pair after 10 minutes of etching with 5 mM HCl at a potential of -1.1 V,  $R_{ext}=1$  k $\Omega$ . The right electrode is completely etched off. (b) SEM picture of PMMA coated electrodes with an opened square, done by electron beam exposure, to prevent a high leakage current.

dissolved gold ions had the tendency to cluster up before reaching the other electrode (Fig. 1.10(a)), especially at high HCl concentrations. We also observed a complete etching off of one electrode at higher concentrations (5 mM), see Fig. 1.10(a).

To reduce the leakage current from ionic conduction, we protected the electrodes with a layer of polymethylmetacrylate (PMMA). The sample was spincoated with PMMA and baked. Electron beam lithography was used to open a square between the electrodes, see Fig. 1.10(b). To harden the PMMA, the sample was baked again after development for one hour at 200 °C. This method prevents also a large etching of the electrodes leading to gold clusters.

- Deionized water: Compared with an electrolyte, pure deionized water has the advantage of omitting an ionic conduction (leakage current). On the other hand, gold cannot be etched easily in water as it is the case for other metals. Although there was a slight effect sometimes, the process was very slow and higher voltages were necessary than with the HCl solution. An example is shown in Fig. 1.11, where (a) represents a SEM image of the electrode pair before etching and (b) after etching and deposition with water at -1.4 V for 30 minutes. The external resistor was 10 k $\Omega$ . One can clearly see that the gold has deposited on the electrode in form of small clusters.

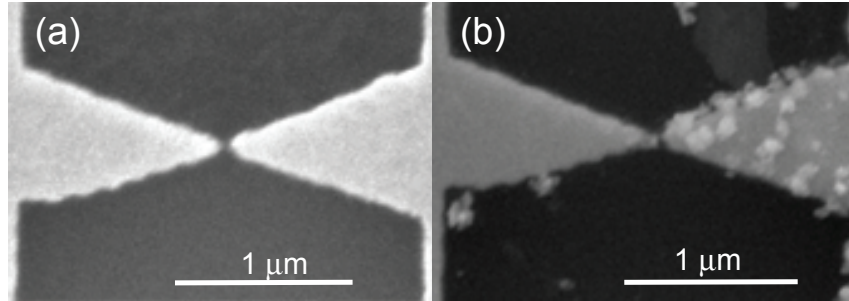


Figure 1.11: SEM pictures of electrodes (a) before etching and (b) after etching and deposition of gold with water.

### 1.3 Discussion and Conclusion

Electrochemical shaping of electrodes is possible to some degree, but it is not easy to control. Working with HCl and with water, the gold ions have the tendency to cluster up before reaching the other electrode. Etching of gold is very hard in water, complexing ions should be tested to avoid this problem.

The deposition from an ionic metal solution is easier, but since the electrochemical deposition leads to metal growth in all directions, the gap can only be decreased at the expense of increasing its lateral dimensions. Low concentrated HCl can be used, but it is important to protect the electrodes with an insulating layer to avoid a large leakage current. This should also be done when the gold solution is used.

Although some results were obtained, this technique was not straightforward enough and offered less advantages than the break junction method. For this reason we decided to discontinue this approach and focused on the break junction, which is subject of the following chapters.



## Chapter 2

# The principle of metallic atomic contacts

Atomic contacts can be obtained by simple experimental techniques. A neck-shaped nanowire is stretched in a controlled manner in order to reduce its diameter down to a single atom. At this stage the electrical conductance of the wire is determined by the nature of the central atom. Atomic contacts have been used intensively to study concepts from mesoscopic physics including conductance quantization, multiple Andreev reflections or shot noise. A very useful feature of atomic contacts is that the breaking process creates rather sharp electrode tips. In addition, the distance between the electrodes is tunable. Therefore atomic contacts prove to be excellent devices for single molecule measurements.

### 2.1 Brief history of atomic-sized conductors

The fundamental step for the exploration of atomic sized contacts came with the invention of the Scanning tunneling microscope (STM) by Binnig and Rohrer in 1981. Gimzewski and Möller used the STM specifically for exploring the transition from the tunneling regime to the point contact [25]. At the same time Moreland *et al.* invented a "Squeezable electron tunneling junction" [26] which after further development resulted in the break junction [27]. Moreland's break junction technique was pursued further by Müller *et al.* in 1992 in order to obtain clean and stable contacts [28, 29]. The name Mechanically Controllable Break Junction (MCBJ) was then coined for this technique. Müller *et al.* reported first results on Pt and Nb contacts where they observed steps in conductance and supercurrent. This phenomenon was attributed to atomic rearrangements in the constriction. In the following years many experiments were realized to study the interplay between quantized conductance and atomic structure [30, 31, 32, 33]. Experiments with a broad variety of metals were investigated. Simultaneous measurements

of force and conductance during the rupture and formation of an atomic contact finally proved that the conductance steps are associated with the atomic rearrangements [34]. In 1997 followed a breakthrough in the understanding of the conductance of a single atom. Scheer *et al.* developed a technique based on the measurement of nonlinear current-voltage characteristics for quantum point contacts between superconducting leads [35]. These nonlinearities are sensitive to the individual transmission channels. By studying different materials they could prove that the number of conductance channels in a single atom contact is determined by the number of valence orbitals of the atom [36].

In 1997 break junctions came into play for the first time in the context of molecular electronics [7]. Break junctions were employed to contact molecules because they allow a relatively simple fabrication of clean metallic contacts at the molecular size. Additionally the distance between the electrodes is tunable and the system offers a high mechanical stability. These advantages lead to a wide use of the break junction for single molecule measurement [13, 37, 38, 39].

## 2.2 Principle and fabrication of atomic sized contacts

### 2.2.1 Scanning tunneling microscope (STM)

The STM was the first technique to create atomic contacts. In the normal mode an STM tip scans over the sample surface without making contact. The distance between tip and surface is held constant by applying a bias voltage and controlling the tunneling current.

Producing atomic contacts with a STM works as shown in Fig. 2.1. The

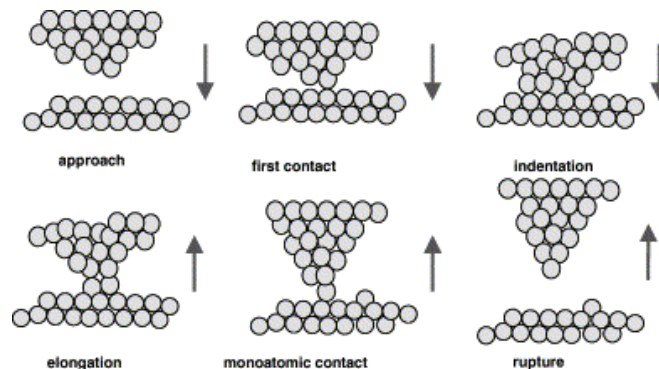


Figure 2.1: (reproduced from [40]): Representation of atomic contact fabrication using an STM.

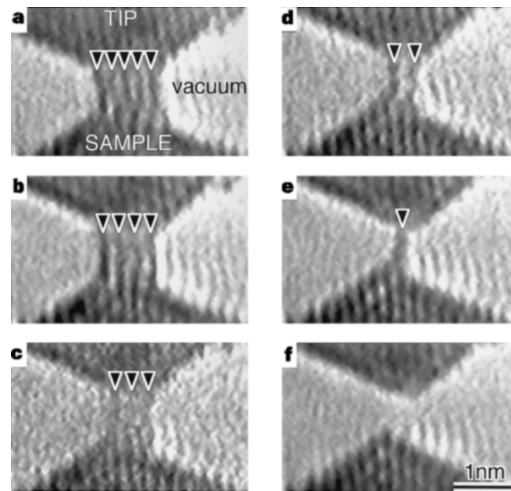


Figure 2.2: (reproduced from [41]): TEM images of a shrinking contact while withdrawing the tip. A gold bridge formed between the gold tip and the gold substrate thinned from **a** to **e** and ruptures at **f**. Dark lines indicated by arrowheads are rows of gold atoms.

tip is pressed against the metallic surface where a large contact is formed (indentation). Subsequently the tip is withdrawn from the surface using a piezoelectric actuator and a neck is formed (elongation). During the entire elongation the conductance is monitored. If the experiment is done with a monovalent metal and the conductance value is of one conductance quantum  $G_0 = 2e^2/h \approx 1/12.9 \text{ k}\Omega$ , a one atom contact is formed before the neck finally breaks. This experiment has been performed at room temperature and at cryogenic temperature, but there was no significant difference observed in the conductance quantization [42, 43].

An experiment by Ohnishi *et al.* [41] shows the structure of the Au neck between the STM tip and the surface by direct observation with a Transmission Electron Microscope (TEM), shown in Fig. 2.2. They could verify that the conductance of a single strand of Au atoms is  $2e^2/h$  and that the conductance of a double strand is twice as large.

### 2.2.2 Mechanically controllable break junction (MCBJ)

The principle of the break junction is a very simple one. A metal wire with a constriction is fixed on top of an elastic substrate. Bending the substrate causes an expansion of the top surface and the wire to break at the constriction. This results in two electrodes which can be brought back into contact by relaxing the force on the substrate.

### The conventional break junction

In order to carry out first test experiments we constructed a simple break junction setup of the conventional type, i.e. with notched gold wires. The principle of a MCBJ is illustrated in Fig. 2.3 where a schematic side view of the mounted sample is shown.

A 0.25 mm thick gold wire is soldered on top of a 3 mm thick epoxy plate with copper contacts. The central part of the wire ( $\sim 2$  mm) is freely lying as shown in Fig. 2.4(a). The notch in the central part is done manually with a scalpel in order to obtain a diameter of about one fourth of the original wire diameter. After a cleaning step in ethanol the sample is mounted in the three-point bending configuration consisting of two counter supports made of copper and the push-rod (Fig. 2.4(b)). The push-rod consists of a micrometer translator with an integrated piezo actuator (P250 PZT from PI). The maximum elongation of the piezo is 20  $\mu\text{m}$ .

While bending the elastic substrate the strain is concentrated in the freely lying section  $u$  on top of the surface (see Fig. 2.3) and the wire breaks. Using the piezoelectric actuator, one can fine control the movement and reach atomic scale of the distance between the electrodes. Fig. 2.5 shows representative conductance traces in units of  $G_0$  versus inter-electrode distance  $d$  when breaking a notched gold wire.

Assuming that the bending is elastic the displacement  $d$  is proportional

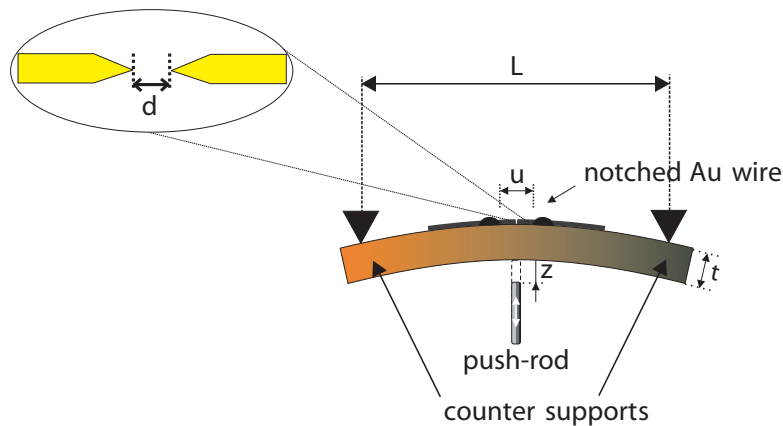


Figure 2.3: Mechanically controllable break junction set-up. A notched wire is fixed on an elastic substrate. While bending the beam the wire breaks and the distance between the resulting electrodes can be adjusted by moving the push-rod. A zoom of the broken wire indicates the inter-electrode distance  $d$ .



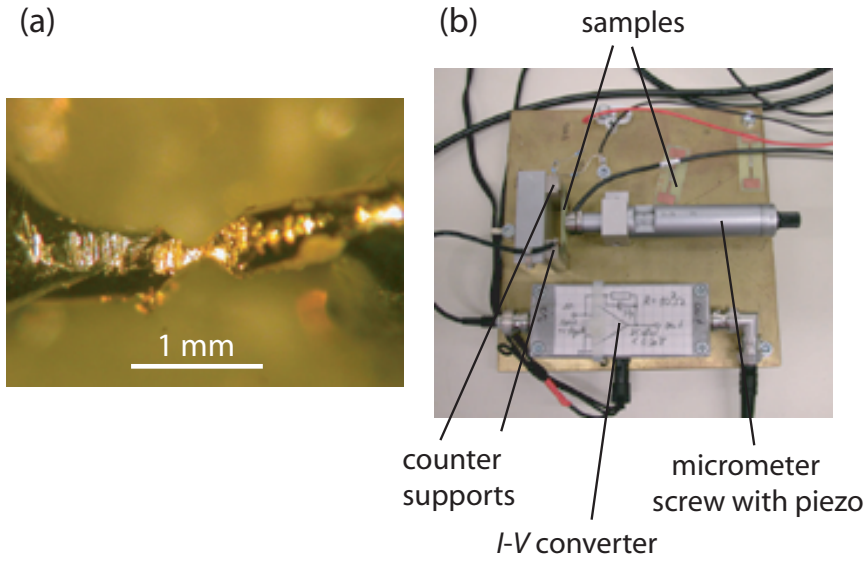


Figure 2.4: (a) A notched gold wire soldered on an epoxy plate with copper contacts. (b) Break junction set-up for hand-notched wires on an epoxy substrate. The central part is bent with a micrometer screw including a piezoelectric element.

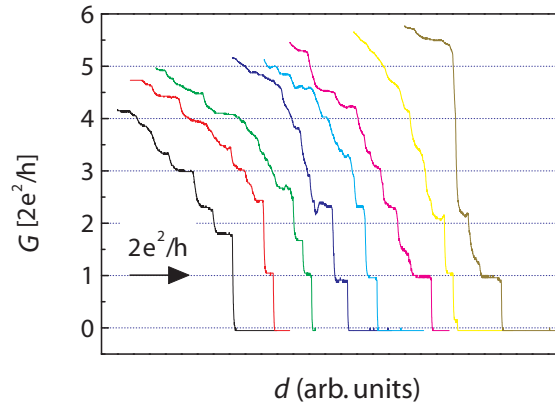


Figure 2.5: Conductance traces in units of  $G_0$  versus inter-electrode distance  $d$  (in arb. units) when breaking a notched gold wire. The curves are shifted horizontally for clarity.

to  $z$ . The ratio  $z/d =: r$  is called the reduction factor and  $1/r =: a$  the attenuation factor. The geometrical attenuation factor  $a_g$  is given by  $a_g = 6ut/L^2$ . The geometry of our samples ( $u=2$  mm,  $t=3$  mm and

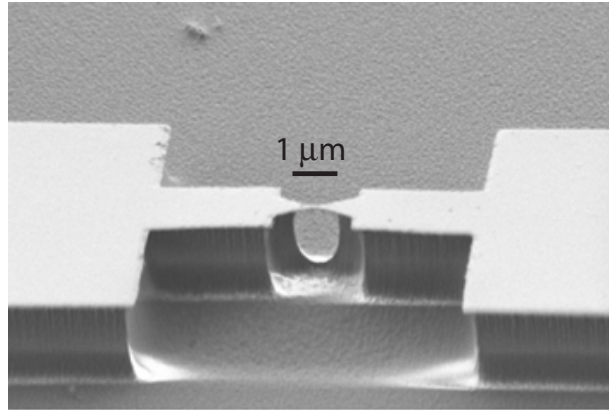


Figure 2.6: SEM image of a microfabricated break junction with the underetched section  $u$ .

$L=35$  mm) results in  $a_g \sim 3 \times 10^{-2}$ . The calculation and the calibration of the attenuation factor is discussed later in this chapter.

### The microfabricated Break Junction

A microfabricated MCBJ on silicon was first presented by Zhou *et al.* [44]. Later the technique was further developed on an elastic substrate (phosphor-bronze) [45]. We constructed a second setup for microfabricated break junctions, which is introduced in chapter 3 where the sample fabrication is explained as well. A SEM picture of a typical junction is shown in Fig. 2.6.

The advantage of this new technique is the reduction of the attenuation factor  $a_g$  by at least two orders of magnitude. In our particular case we achieve  $a_g \sim 10^{-6}$ . The consequence of the reduced attenuation factor is a higher immunity to external vibrations and drifts [45]. Another advantage of the microfabricated break junction is the possibility to design the environment of the atomic contact. A piezo element is not used in our setup due to the limited range of expansion and the high reduction factor  $r$  which results in a very small elongation on top of the surface ( $< 1$  Å). Therefore a mechanical gear system in combination with a stepper motor is integrated in the set-up.

### Calibration of the attenuation factor

The inter-electrode separation is an important parameter in context of measuring molecules. Therefore the exact value of the attenuation factor  $a$  is needed, which is not easy to obtain. For an elastically homogenous system  $a$  can be derived based on geometrical considerations. Using the

standard elastic beam theory [46] it has to be distinguished between a beam with supported ends and a beam with fixed ends, giving rise to different curvatures. A beam with supported ends (our case) leads to an attenuation factor  $a_g = 6tu/L^2$  whereas a beam with fixed ends gives rise to  $a_g = 12tu/L^2$ . Another possibility to calculate  $a_g$  is to compare the curvature of the beam with the one of a segment of a circle, leading to  $a_g = 4tu/L^2$ . Thus, depending on the approach,  $a_g$  can differ by a factor of 3. Based on our geometry with values  $t=0.3$  mm,  $u \sim 1$   $\mu\text{m}$  and  $L=20$  mm and taking the expression  $a_g = 6tu/L^2$ , we estimate  $a_g \approx 5 \times 10^{-6}$ .

To verify this formula we made the following procedure. By moving the push-rod in  $z$  direction, we elongate and finally break the constriction of a break junction. After the breakage, we measured the conductance versus distance  $d$  of the junction in vacuum in the open state, i.e. in the tunneling regime (conductance  $G$  between  $4 \times 10^{-5}$  and  $0.01 G_0$ ). An example of such a measurement is shown in Fig. 2.7 with the tunneling current  $I$  versus vertical movement  $z$  of the push-rod. We then take the expression for the tunneling current at low bias through a square barrier of height  $\phi$  and thickness  $d$ ,  $I \propto \exp[-2d\sqrt{2m\phi}/\hbar]$  where  $m$  is the electron mass and  $d = a(z - z_0)$  the distance between the two extremities of the Au contacts on either side. We then have  $\ln(I) \propto -Bz + \text{const.}$ , where  $B = 2a\sqrt{2m\phi}/\hbar = 1.025[\text{eV}^{-0.5} \text{\AA}^{-1}]\sqrt{\phi}$  a. Hence the slope of  $\ln(I)$  vs.  $-z$  is given by  $B \propto a\sqrt{\phi}$ . If we use the measured  $B$  for vacuum and fix  $\phi_{vac}$  to the established value of 3.5-5.0 eV [25], we

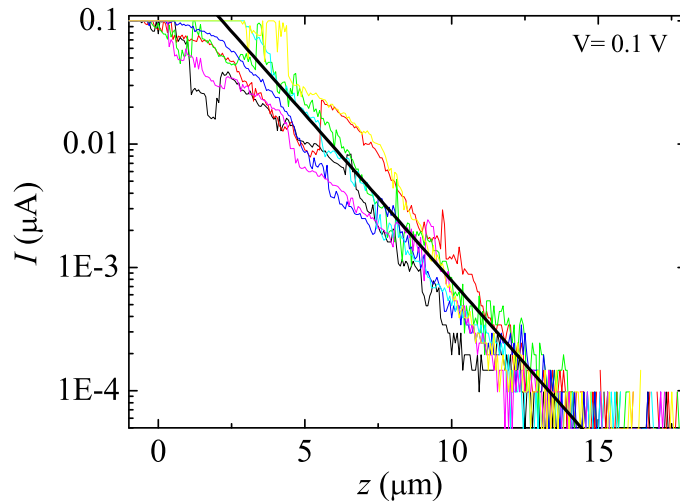


Figure 2.7: Measurements of the tunneling current  $I$  versus vertical movement  $z$  of the push-rod in vacuum. The black line is the slope  $B$  obtained from the fit of  $I$  to an exponential law, i.e.  $\ln(I) = -BI + \text{const.}$

get  $a \simeq 5 \times 10^{-5}$ , one order of magnitude larger than  $a_g$ .

We performed the same fit ( $\ln(I) \propto -Bz + \text{const.}$ ) for several samples measured in air and found differences up to a factor of 5 in  $B$ . Fig. 2.8 compares the geometrical attenuation factor  $a_g$  and the slope  $B$  for several gold junctions. There is a certain correlation between the two factors and in fact, both magnitudes are always very similar for junctions on the same sample (77b and 77c, 79a and 79c, 83a and 83b). This is not surprising as the substrate thickness and the width of the underetched part enter in the equation for the geometrical reduction factor. These two magnitudes are the same for junctions on the same sample. In spite of the partial correlation between  $a_g$  and  $B$ , their values intersect several times from one sample to the other, i.e.  $B$  is not proportional to  $a_g$ . These substantial deviations are likely due to plastic deformation of the substrate.

Although the formula for  $a_g$  is widely used, it ignores the fact that the substrate can plastically deform and that the polyimide flows in the vicinity of the junction due to inhomogeneous stress [40, 47]. A three-dimensional finite element analysis to investigate the mechanics of lithographically defined break junctions was done by Vrouwe *et al.* [47]. They found that  $a_g$  should be corrected by a significant factor  $\xi = 2 - 4$  ( $a = \xi \cdot a_g$ ) due to inhomogeneous stress in the structured polyimide layer, what changes the bending mechanism. The presence of plastic

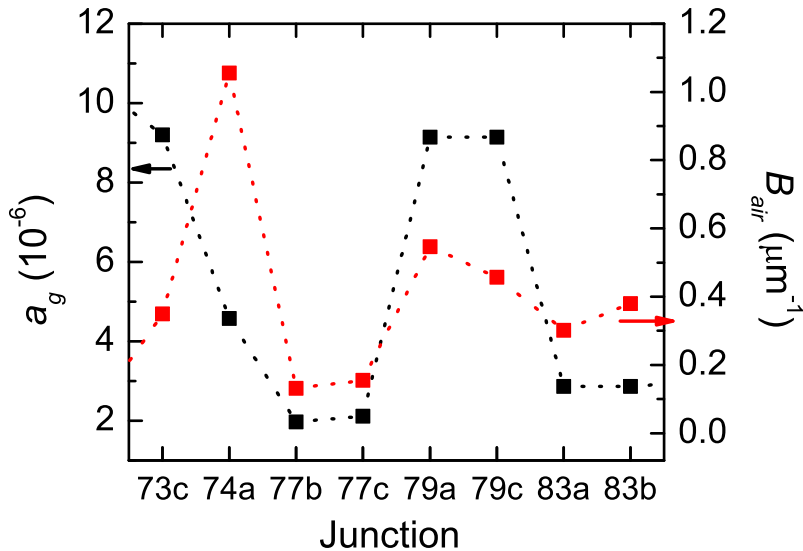


Figure 2.8: Attenuation factor  $a_g = 6tu/L^2$  and  $B = 2a\sqrt{2m\phi}/\hbar$  (in air) for 8 different junctions.

deformations is confirmed by a residual bending of the substrate after several loading and unloading cycles in some experiments. Moreover, we estimate that a vertical displacement  $z$  of  $\sim 1$  mm, a typical excursion needed to break the junction, is sufficient to reach the tensile strength of phosphore bronze ( $\sigma_{max}=300-700$  MPa). Plastic deformations change the bending geometry and can substantially increase the mechanical reduction factor, thus  $a \neq a_g$ . For the extreme case we assume a triangular shape of the substrate instead of a uniform bending as it is shown in Fig. 2.9(a), the phosphore bronze substrate is plastically deformed at this stage. The maximal stress of polyimide ( $\sigma_{max}(\text{polyimide})=6 \cdot 10^6$  Pa) is two orders of magnitude smaller than the one for phosphore bronze, leading to  $z_{max} \leq 0.2$  mm. As the vertical displacement  $z$  during the experiment exceeds 0.2 mm, we consider the limiting case in which the polyimide (and the junction on top) acts like a hinge when moving the push-rod (see Fig. 2.9(a)). It is opening and closing by an amount  $x$  at the top point. For this case we can calculate the plastic attenuation factor  $a_p = x/z$  by simple trigonometric equations (the illustration to the following equations is shown in Fig. 2.9(b)) resulting in

$$x = 2d \frac{z}{\sqrt{(L/2)^2 + z^2}}. \quad (2.1)$$

If  $z \ll L/2$ , we can work with the approximated expression

$$\delta x = 4 \frac{d}{L} \delta z. \quad (2.2)$$

By taking  $d = t_p$ , where  $t_p$  is the polyimide thickness and  $L=20$  mm, we get  $a_p = \delta x / \delta z = 6 \times 10^{-4}$ , i.e. 2 orders of magnitude higher than the

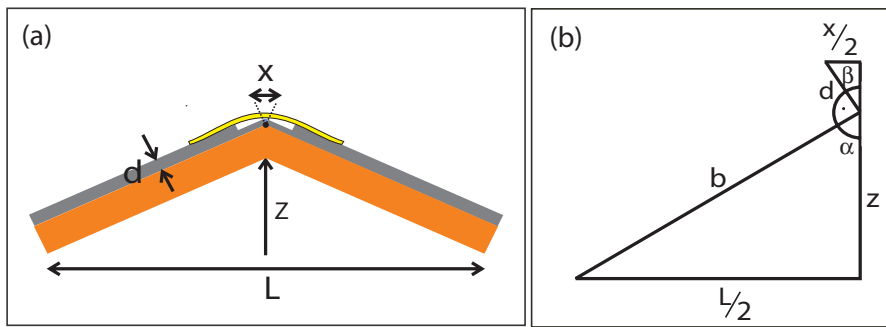


Figure 2.9: (a) Sketch of a strongly bent sample which is plastically deformed displaying a residual curvature after several loading and unloading cycles. The polyimide acts like a hinge when moving the push-rod and is opening and closing by an amount  $x$  at the top point. (b) Illustration to calculate the attenuation factor of a plastically deformed sample.

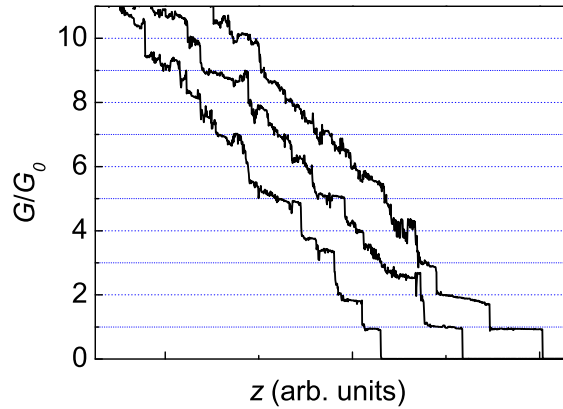


Figure 2.10: Conductance curves (normalized to  $G_0$ ) versus vertical displacement of the push-rod  $z$  while opening a gold junction. The curves are shifted horizontally for clarity.

reduction factor  $a_g$  calculated in the fully elastic case and one order of magnitude higher than the value obtained with the fit discussed previously. These comparisons reveal the importance of a proper calibration of  $a$  in order to calculate the distance between the two electrodes.

A very accurate method to calibrate the distance between MCBJ electrodes in UHV was introduced by Kolesnychenko *et al.* [48]. They used the tunnel conductance oscillation effect (Gundlach oscillations or field emission resonances) at  $eV \geq \phi$ , where  $e$  is the electron charge,  $V$  the applied voltage and  $\phi$  the workfunction of the metal.

## 2.3 The conductance of atomic sized metallic contacts

### 2.3.1 Conductance steps

To study the conductance of atomic contacts the two metal electrodes are brought in contact and broken again repeatedly. Fig. 2.10 shows examples of conductance curves in units of  $G_0$  versus vertical displacement of the push-rod  $z$  while breaking a gold junction at room temperature. Recognized are series of plateaus in the conductance, the most pronounced one is of the order of  $1G_0$ . While the last plateau is nearly horizontal the ones at higher conductance values exhibit a slightly negative slope. At the end of each plateau a sharp jump is observed at which the conductance decreases by an amount of the order of  $1G_0$ . These sharp steps are explained by atomic rearrangements resulting in a step-wise variation of the contact diameter [28]. A very nice experiment was done by Rubio *et al.* [34] with a combined STM-AFM (see Fig. 2.11).

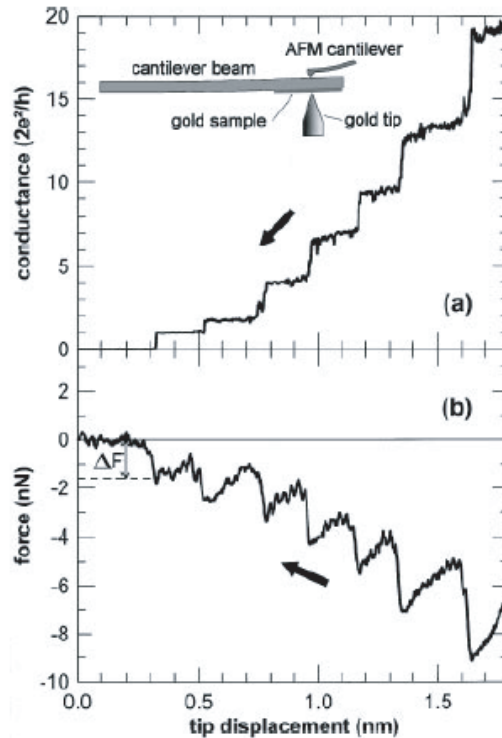


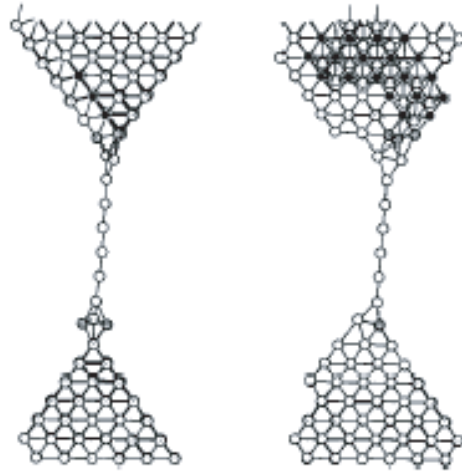
Figure 2.11: (reproduced from [34]): Inset: Schematic representation of the set-up combining an STM with an AFM. Simultaneously measured conductance (a) and force (b) during elongation and rupture of an atomic-sized constriction at 300 K.

By measuring simultaneously the force and the conductance they could show that on a plateau the atomic configuration is only elastically deformed, while a conductance jump is correlated with mechanical force relaxation and consequently, with atomic rearrangements.

Molecular dynamics simulations [49, 50, 51, 52] confirm the experimental observations and provide a detailed description of the evolution of the atomic structure of metallic nanocontacts and of the mechanical deformation processes taking place during an elongation process. They describe a period in which the wire stretches elastically, with a smooth, approximately linear force increase while the conductance and the cross section decrease. After a certain elongation, when the tension in the wire has reached a high level, the system becomes mechanically unstable and the atoms rearrange themselves into a different structure. This is accompanied with a sharp decrease in the force and in the conductance. The pattern is repeated until the wire eventually breaks.

A very remarkable feature of the simulation is the formation of an unusually long chain of single atoms in the middle of the contact of Au[100]

Figure 2.12: (reproduced from [52]): Snapshot of atomic configurations of a Au[100] nanocontact from MD simulations from two different viewpoints.



shown in Fig. 2.12. As a result there is a plateau in the conductance at  $1 G_0$  over an elongation length of about  $10 \text{ \AA}$ . The remarkable length of the atomic gold chain and the interatomic distance has been measured by Untiedt *et al.* [53]. Using a precise calibration procedure they find the mean value of the interatomic distance before the chain rupture to be  $2.5 \pm 0.2 \text{ \AA}$ , and plateaus up to  $1.5 \text{ nm}$  corresponding to 6 atoms. The conductance never exceeds  $1 G_0$  confirming that the chain acts as a one-dimensional quantized nanowire with the ability to support ballistic electron transport.

The structural rearrangement of the contacts is varying each time the contact is pressed together and opened again. Therefore the conductance traces are different in each measurement. The only reproducible trace is the plateau at  $1 G_0$  corresponding to one atom or a chain of atoms. This feature is typical for monovalent metals like Au, Ag, Cu and for the alkali metals. Often the plateaus are not located at exactly integer quantum values. Such deviations are attributed to back scattering on defects near the contact.

Fig. 2.13 presents three typical conductance traces obtained when bringing the gold contacts together. The tunnel current increases first exponentially with the distance. When the two metal surfaces are closed a jump to contact occurs, first observed by Gimzewski and Möller [25]. Afterwards the conductance increases in a staircase-like manner but with less plateaus than in the breaking curve (Fig. 2.10). The first contact is usually of the order of several  $G_0$  and only rarely at  $1 G_0$ . This tendency to make bigger than one-atom contacts when bringing the electrodes back to contact is well known from experiments [54, 55]. This sudden jump-to-contact mechanism has been studied theoretically and



the picture that has emerged is the following [56, 57]: When two surfaces are brought close to each other, the system becomes unstable at a certain critical distance of a few angstroms, and the surfaces suddenly jump into contact. This is called “adhesive avalanche” and involves a collective motion of many atoms. Sørensen *et al.* [58] suggest another mechanism, called “diffusion-to-contact”, where contact formation occurs by a thermally activated sequence of atomic hops.

Gold is the most used metal for atomic-sized contacts and therefore also the most widely studied. But besides gold, steps have been observed for a wide variety of metals under various experimental conditions [40]. The issue of different metals is briefly addressed in chapter 3.3.3.

### 2.3.2 Conductance histograms

In order to perform a statistical analysis of the data, it is useful to construct conductance histograms from a large set of conductance versus displacement curves. Since the atomic-scale contact configuration is different for each opening and closing cycle, each conductance trace is unique. The peaks in the histogram correspond to conductance values that are preferred by the atomic system. Fig. 2.14 shows two examples of conductance histograms from a gold break junction in air, one built from 100 opening curves (a) and one from 100 closing curves (b). The most striking feature in Fig. 2.14(a) is the peak at  $1 G_0$  as expected for monovalent wires [36]. It results from the formation of a chain of gold atoms during the last stage of contact breaking. There are two other clear peaks near  $2 G_0$  and  $3 G_0$ , both clearly shifted to somewhat lower values compared to exact multiples of  $G_0$ . As mentioned in the previ-

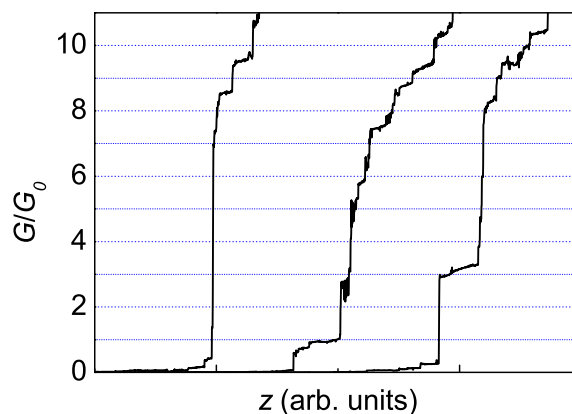


Figure 2.13: Conductance curves (normalized to  $G_0$ ) versus vertical displacement of the push-rod  $z$  while closing a gold junction. The curves are shifted horizontally for clarity.

ous section, this shift is attributed to backscattering of the electrons. The features beyond a conductance value of  $3 G_0$  are rather broad and unclear, but there is a report of individual peaks at 4 and  $5 G_0$  [43] measured with an STM at 4 K. There are no qualitative changes in the histograms at different temperatures but the relative height of the first peak grows towards lower temperatures [40].

Contaminants can influence the stability of the  $1 G_0$  plateau. This was shown by Hansen *et al.* [59] in a STM experiment, where they found less stable single-atom contacts with ultra clean contacts compared with contaminated contacts. There is a rule of thumb telling that the cleaner the conditions are at room temperature the more difficult it is to create stable atomic contacts [55].

The histogram constructed from the closing curves shown in Fig. 2.14(b) exhibits only little features. There is still a peak at  $1 G_0$  and two small but very broad features at around 2 and  $3 G_0$ . The peak at zero conductance arises from the accumulation of points in the tunneling regime.

### 2.3.3 Conductance of a single atom

The conductance value of a single-atom contact depends on the material. Monovalent metals like Au, Ag, Cu and alkali metals reveal a dominant peak in the conductance histogram at, or just below  $1 G_0$ . Transition metals with partially filled d-shells are characterized with a single broad peak well above  $1 G_0$  but not at an integer value of conductance. What is the source of these different features? Or what defines the conductance of an atomic point contact?

The conductance of structures with dimensions much smaller than the phase coherence length is given by the Landauer expression

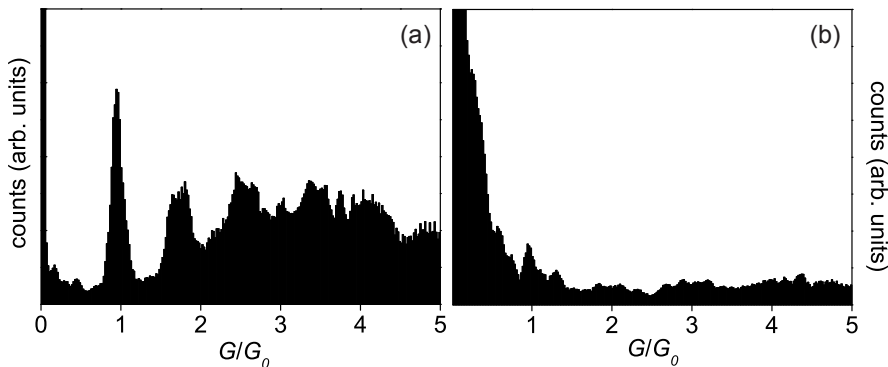


Figure 2.14: Conductance histograms, collected from 100 measurements of  $G(z)$  versus  $z$  for Au while (a) opening and (b) closing the junction. The histograms are normalized by the total number of counts. Bin width:  $0.02 G_0$ .

$$G = G_0 \sum_n \tau_n, \quad (2.3)$$

where  $G_0 = 2e^2/h$  is the conductance quantum ( $e$  is the electron charge and  $h$  the Planck's constant) and  $0 < \tau_n \leq 1$  describes the transmission probability of the  $n$ th conductance channel. A deeper understanding of the nature of conductance through a single atom requires the knowledge of  $\tau$  for all individual channels.

A technique developed by Scheer *et al.* [35, 36] determines the number of conduction channels of the last contact using the non-linear current-voltage characteristics of superconducting constrictions. These nonlinearities are called 'subgap structure'. The experiments included metals with different valence structure and revealed a direct link between valence orbitals and the number of conductance channels in a one-atom contact. It was found that for  $s$ -metals (Au) only one conduction channel contributes to the conductance at the lowest conductance plateau.  $sp$ -metals (Al, Pb) contribute with 3 channels while transition metals (Nb), possess five conduction channels ( $s$ - and  $d$ -orbitals). Fits to the measured  $I$ - $V$  curve allowed to deduce the transmissions of the individual channels. Both the number of the channels and the value of the transmission probability were in good agreement with tight binding calculations [60].

Consequently this experimental and theoretical work could prove that the smallest contact is indeed formed by a single atom and that the electrical transport properties are determined by the chemical valence of the involved atom.



## Chapter 3

# Sample preparation and description of the setup

More advanced break junction devices make use of microfabrication techniques to define the metal bridge. This method provides the advantage of a higher stability against external vibrations and the possibility to design the structure. As flexible substrate serves a sheet of phosphore bronze or spring steel covered with an insulating polyimide layer. The top of the substrate is patterned with a combination of UV- and e-beam lithography and metal is evaporated through the obtained mask. The last step includes an isotropic dry etching to free the narrow bridge from the polyimide resulting in a freestanding metallic bridge.

### 3.1 Substrate preparation

As substrate serves a 0.3 mm thick phosphore bronze sheet (Cu 94%, Sn 5%, Ni 0.2%, Zn 0.2%, Fe 0.1%, Pb 0.02%, P 0.01-0.4%), which has to be polished first. For this purpose the sheets are cut in  $5 \times 5$  cm pieces and polished with a manual polisher. Diamond suspension (Metadi Supreme Polycrystalline from Bühler GmbH) with particle sizes from  $9 \mu\text{m}$  down to  $1 \mu\text{m}$  together with a lubricant for diamond polishing (Metadi fluid from Bühler GmbH) are used as polishing auxiliary. The wafers are cleaned in a soap solution followed by acetone and isopropanol baths at ultrasonic agitation. Then the metallic substrate is spin coated with a Pyralin adhesion promoter (VM 651 from HD Microsystems) for 40 s at 2000 rpm. The adhesion is improved by baking the substrate for 1 minute on a hot plate at  $110 \text{ }^\circ\text{C}$  (the adhesion promoter turned out to be redundant later). Then a  $\sim 3 \mu\text{m}$  polyimide layer (Pyralin PI2610, HD Microsystem) is spun on the substrate in two steps, first for 40 s at 500 rpm and subsequently for 40 s at 2000 rpm. To complete the imidization of the polyimide, the wafers are baked in the oven at  $200 \text{ }^\circ\text{C}$  for 30 minutes. A second layer of polyimide is spun on the substrate to reduce the probability of shorts through the polyimide. After another

baking at 200 °C for 30 minutes the substrate is annealed for one hour at 380 °C and  $10^{-5}$  mbar. Finally, the coated substrate is cut in  $24 \times 10$  mm samples.

The polyimide is used for three reasons. First, it planarizes the phosphore bronze surface and second, it serves as an insulating layer between the metallic pattern on the top of the polyimide and the substrate. Finally, the polyimide can be dry etched to get a free standing bridge (see Section 3.3).

Phosphore bronze gets easily plastically deformed (discussed in the previous chapter). Spring steel is a material with a higher tensile strength limit and therefore also used as break junction substrate. On the other hand it has the disadvantage, that it is more difficult to polish due to its hardness.

## 3.2 Lithography and metal deposition

### 3.2.1 Principle

Optical and e-beam lithography are standard methods in microelectronics for patterning a substrate. They are based on the same principle: The substrate is spin-coated with an organic resist, which is polymerized on the hot plate or in the oven. The exposure to light or to the electron beam leads to a change in the solvability of the affected area. With a positive resist the exposed area is dissolved during the development, whereas negative resist is further polymerized by the exposure and the unexposed area can be dissolved.

### 3.2.2 Optical lithography

In optical lithography the light passes an optical mask which consists of a metal film on glass. The exposure time is small and independent of the surface area and in general, the method is fast and relatively cheap. The resolution is restricted by the wavelength of the light.

As resist serves a negative photoresist (ma-N-415 Micro Resist Technology, Germany). After spin coating it is baked on the hot plate at 90 °C for 90 s. A mask aligner MJB 3 (Karl Süss, Germany) with a Hg lamp is used for the exposure. The exposure time is 20-25 s. A developer (ma-D-332S from Micro Resist Technology, Germany) is used to remove the unexposed area. The development time is 80 s, afterwards the sample is rinsed in water.

### 3.2.3 Electron beam lithography

Electron beam lithography is a much more complex method and more time consuming than UV lithography. A scanning electron microscope

(SEM) is used to pattern the resist. The mask is designed on the computer and transferred to the microscope. The resolution is given by the size of the beam and the proximity effect.

A standard positive resist (PMMA, Polymethylmetacrylate 950 K from Allresist) is diluted with additional chlorbenzene to decrease the resist thickness ( $\sim 300$  nm), spin coated on the substrate (4000 rpm, 40 s) and baked in the oven at  $200$  °C for 40 minutes. It is exposed using a JEOL JSM-IC 848 scanning electron microscope. The stage and the pattern generation is controlled with the software Proxy-writer or Elphy Quantum from Raith GmbH. The development is done in a solution of MIBK (4-Methyl-2-pentanone): IPA (Isopropanol) 1:3 for 45 s. The sample is then rinsed for 30 s in IPA to stop the development.

### 3.2.4 Metal deposition

After development the resist layer serves as a mask for the metal deposition. This step takes place in a vacuum chamber (PLS 500 from Balzers) at  $\sim 10^{-6}$  mbar. The sample is mounted on a tiltable sample holder allowing evaporation at different angles. In addition, the sample holder can be cooled with liquid nitrogen to improve the adhesion of the metal. The metal is thermally evaporated by an electron gun. The thickness of the evaporated film is controlled with a calibrated quartz resonator. Once the metallic film is evaporated, the sample is immersed in acetone to remove the PMMA mask. The acetone can be warmed up to improve the lift-off.

## 3.3 Plasma etching

In the final step, the polyimide is isotropically dry etched to obtain a suspended central metal bridge. This is done by Reactive Ion Etching (RIE) in a PlasmaLab 80 plus (Oxford) under the following rf plasma

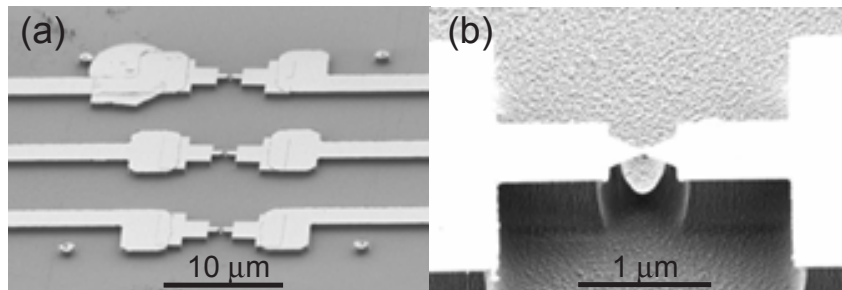


Figure 3.1: SEM picture of a sample with three junctions in parallel (a) and a suspended gold nanobridge (b).

conditions: a flow of 32 sccm of oxygen and 8 sccm of  $\text{CHF}_3$  at a pressure of 0.025 torr and a power of 100 W. The etch rate is  $\sim 100$  nm per minute. The final device is inspected with a Scanning Electron Microscope (LEO Supra 35), see Fig. 3.1. On a substrate, three junctions with a central constriction of 80-150 nm width are fabricated in parallel. The resistance of a junction ranges typically between  $150 \Omega$  and  $300 \Omega$ .

### 3.4 The setup

The sample is mounted (unclamped) in the setup with a three-point-bending mechanism, sketched in Fig. 3.2. A picture of the mounted sample is shown in Fig. 3.3. The distance between the two counter-supports is 20 nm. The vertical displacement of the push-rod is driven by a stepper motor (Phythron GLD) via a coupling gear, allowing for displacement amplitudes up to a few millimeters. One full turn of the worm wheel moves the push-rod 1 mm in the vertical direction. The worm gear pair has a reduction of 1:50 whereas the planetary gear exhibits a 1:4 reduction. The motor makes 200 steps for one turn of the gear, whereas 1 step is electronically divided in 8 substeps. Therefore, one step corresponds to 25 nm ( $1/40000$  mm) and one substep to 3.125 nm ( $1/320000$  mm). The motor is controlled by the PC through a serial port RS 232. The motor speed can be adjusted between 500 and 10'000 substeps per second.

To perform measurements in liquid we integrated a liquid cell as shown in Fig. 3.3. It is formed by a portion of a *Viton*<sup>®</sup> tube enclosing a volume of 250  $\mu\text{l}$ . The cell includes an inlet and outlet port (*Teflon*<sup>®</sup> tubes) allowing the exchange of fluids in the course of the measurements. A tight contact of the cell to the sample surface is ensured via a spring. The measurements are performed in a two-probe configuration, using spring-loaded metallic tips. A 12 bit standard data acquisition board (National Instruments) is used both to apply a constant bias voltage and to record the current in the junction as measured by a current-voltage converter with an adjustable gain of  $10^5$ - $10^7$  V/A. The resolution of the DAQ board for an input range of  $\pm 10$  V is 5 mV. An external resistance  $R=1 \text{ k}\Omega$  is used to limit the current in the circuit. The grounding of the measurement setup is provided via the DAQ board source whereas the input is floating, see Fig. 3.4. The entire setup is isolated from the grounded support. To avoid ground loops we inserted an isolation between the lateral shield of the setup and the grounded isolation of the BNC connectors, as sketched in Fig. 3.4. During the measurements we shielded the setup with an aluminium cover. The typical current fluctuations were of  $10^{-10}$  A at 0.1 V<sub>bias</sub>.



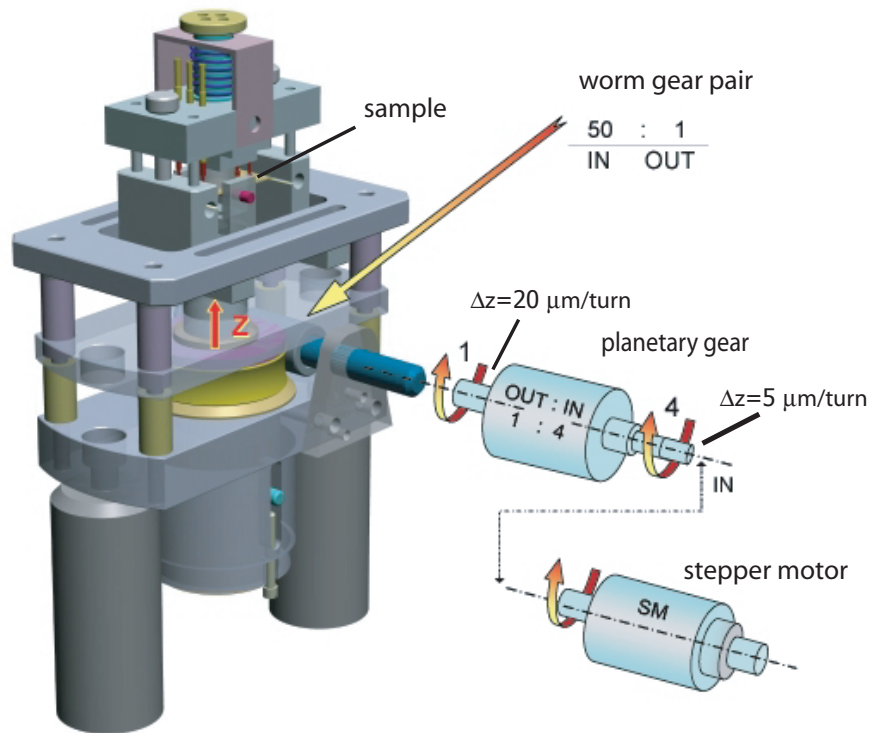


Figure 3.2: Break junction measurement setup

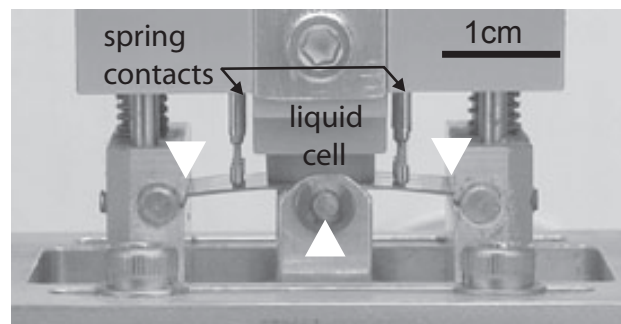


Figure 3.3: Detailed view of the substrate mounted in the three point bending mechanism (white triangles) with a liquid cell pressed against the substrate.

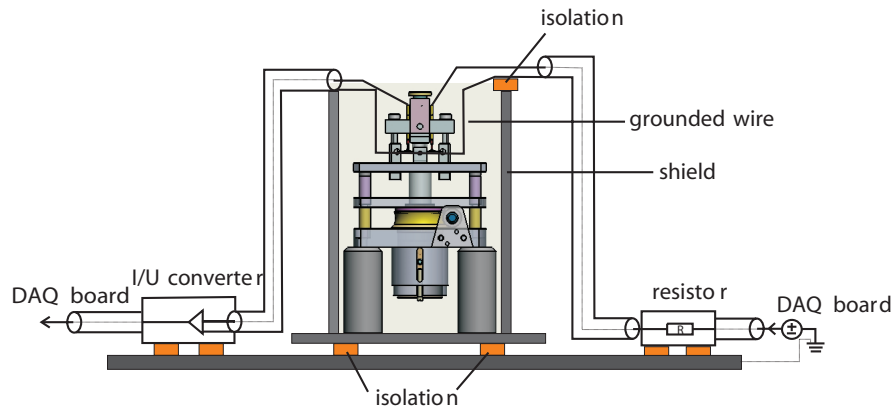


Figure 3.4: Break junction measurement setup with the grounding schematics.

## Chapter 4

# Measurements of atomic contacts in liquid environment

### 4.1 Introduction

Our break junction setup with the integrated liquid cell allows to explore the influence of solvents on the electronic properties of atomic contacts. We studied the variation of the electrical conductance  $G$  of Au junctions with their elongation in the regime of tunneling (low conductance) and true metallic contact (high conductance). As solvents, we have used deionized water, dichloromethane (DCM), dimethylsulfoxide (DMSO), octane and toluene. The last four are of particular interest since they are potential organic solvents for molecules relevant in molecular electronics. In addition, these solvents cover a broad range of polarities. We also compare the results with reference measurements obtained in vacuum and air.

### 4.2 High conductance regime

For the measurements in the high conductance regime the junction was opened and closed to its initial or almost initial resistance value ( $\sim 200 \Omega$ ). For each environment, we collected 100-130 curves of the decrease of the conductance as a function of the vertical displacement  $z$  of the push-rod while extending and, eventually, breaking the constriction. The applied bias voltage was 0.1 V. Fig. 4.1(a) shows typical conductance traces (normalized to  $G_0$ ) versus vertical displacement  $z$  of the push-rod recorded in air. In agreement with previous work in air, vacuum and at low temperature (He), the curves display plateaus at different conductance values. The clearest plateau here is close to  $1 G_0$  as expected for monovalent metals [36] and gives rise to a clear peak in the histogram shown in Fig. 4.1(b). The cause for this feature is discussed

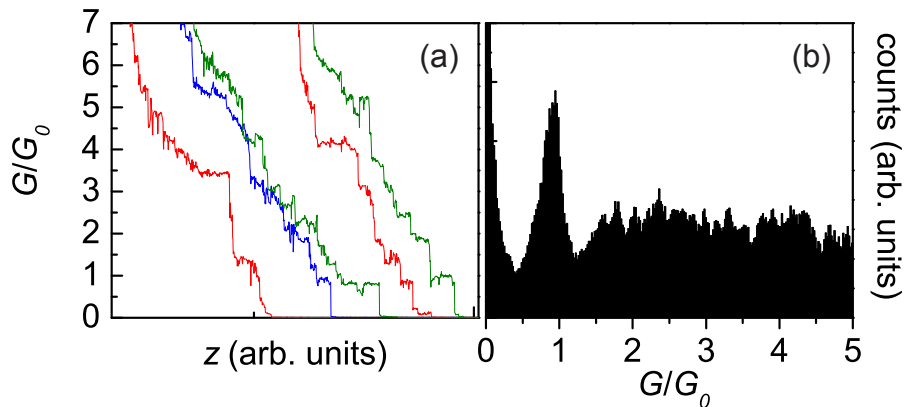


Figure 4.1: (a) Typical conductance curves versus vertical displacement  $z$  measured in air when opening a gold break junction and (b) the corresponding histogram from 100 conductance curves. Bin width is  $0.02 G_0$ .

in Chapter 2.

The same measurements were repeated in the presence of different solvents as well as in vacuum. Fig. 4.2(a) shows conductance curves in DMSO and in toluene whereas Fig. 4.2(b) represents conductance histograms of three different junctions in several environments. Each histogram is built from all the conductance traces measured in one environment and normalized by the total number of counts. The bin width is  $0.02 G_0$ . It was not possible to investigate one junction in all the environments. Therefore, the data for DMSO, octane and toluene correspond to one junction, those for air and water to a second and those for vacuum to a third one. In the conductance regime covered by the measurements, no striking differences between the environments can be observed. Hence the environment plays a minor role in the electronic properties of atomic contacts in the high conductance regime.

### 4.3 Tunneling regime

We now focus on the behaviour of the junctions in the tunnelling regime ( $G$  between  $4 \times 10^{-5}$  and  $0.01 G_0$ ). Several sets of 10 consecutive open-close cycles (up to a conductance of a few  $G_0$ ) were recorded for the same junction in different environments. Fig. 4.3 shows two typical sets of measured curves in a semi-log representation, one recorded in air (a) and one in toluene (b) when the junction was being closed. Subsequent curves show little variation and exhibit a well defined linear regime in a semi-log representation. At higher currents, we observe sometimes curve-to-curve variations that can be attributed to differences in the

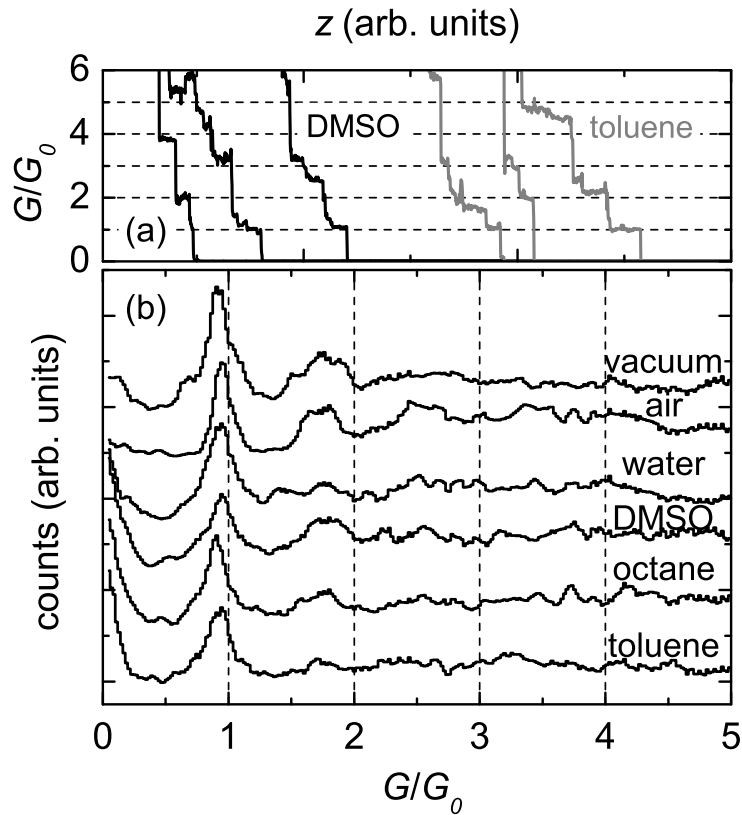


Figure 4.2: High conductance regime: (a) Conductance curves versus vertical displacement of the push-rod  $z$ , shifted horizontally for clarity, for one gold junction in DMSO and in toluene. (b) Conductance histograms, collected from 100 measurements of  $G(z)$  of three junctions measured in different environments. The data for DMSO, octane and toluene correspond to one junction, those for air and water to a second one and those for vacuum to a third one. The histograms are shifted vertically for clarity.

microscopic configurations of the junctions. We chose the closing curves because these are the relevant curves in the perspective of capturing molecules.

We again consider the simple expression for the tunnelling current (see chapter 2) at low bias voltage through a square barrier of height  $\phi$  and thickness  $d$ ,  $I \propto \exp[-2d\sqrt{2m\phi}/\hbar]$  with  $d = a \cdot z$ . To reduce the effect of fluctuations, the slope  $B$  ( $B = 2a\sqrt{2m\phi}/\hbar$ ) was deduced in the low current regime using all 10 curves of each set of measurements simultaneously (two such measurement sets are shown in Fig. 4.3 (a) and (b)). The range for the fit was chosen manually. Curves which deviated strongly from the others were not considered for the fit. The black

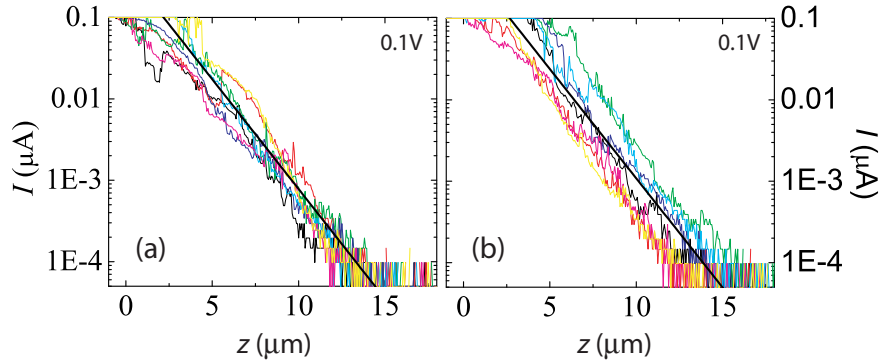


Figure 4.3: Raw data for the current versus the vertical displacement of the push-rod  $z$  measured in (a) air and (b) in toluene in the tunneling regime. The black lines are obtained from fits of  $I$  to an exponential law, i.e.  $\ln(I) = -BI + const.$

lines in Fig. 4.3 (a) and (b) represent the exponential fit with the slopes corresponding to the averaged values of  $B$  for each environment.

Fig. 4.4(a) shows representative raw curves obtained in different environments when the junction was being closed. The lines correspond again to the averaged value of  $B$  for each environment. Whenever measuring in a medium different from vacuum, a clear decrease of the slope is observed which is different in each environment. The decrease of the slope is not correlated with the order in which the environments were tested (and hence, with a possible accumulated contamination of the junction). For the junction of Fig. 4.4 (a) the measurement sequence was: vacuum, octane, air, toluene, DCM and DMSO. The values of  $B$  obtained from several measurement sets are plotted in Fig. 4.4 (b) for the same junction as in Fig. 4.4 (a).

We performed the same analysis for three additional samples and found differences up to a factor of 5 in  $B$  for a given environment (also shown in Chapter 2, Fig. 2.8). This large scattering cannot be assigned to  $\phi$ , because unphysically large barrier heights would then result. The scattering is therefore likely due to sample-to-sample variations in the mechanical attenuation factor  $a$  (see Chapter 2). This is clarified with Fig. 4.5 which illustrates the ratio  $(B/B_{air})^2$  for each environment and for four different junctions. The scattering is strongly reduced here, as the ratio  $(B/B_{air})^2$  is directly proportional to the ratio of the effective barrier heights and does not depend on  $a$ . In addition, there is a clear tendency in the ratio  $(B/B_{air})^2$  when comparing the different environments. Therefore,  $\phi$  does depend on the environment in a specific and reproducible way.

In the following, I would like to summarize some theoretical proposals for

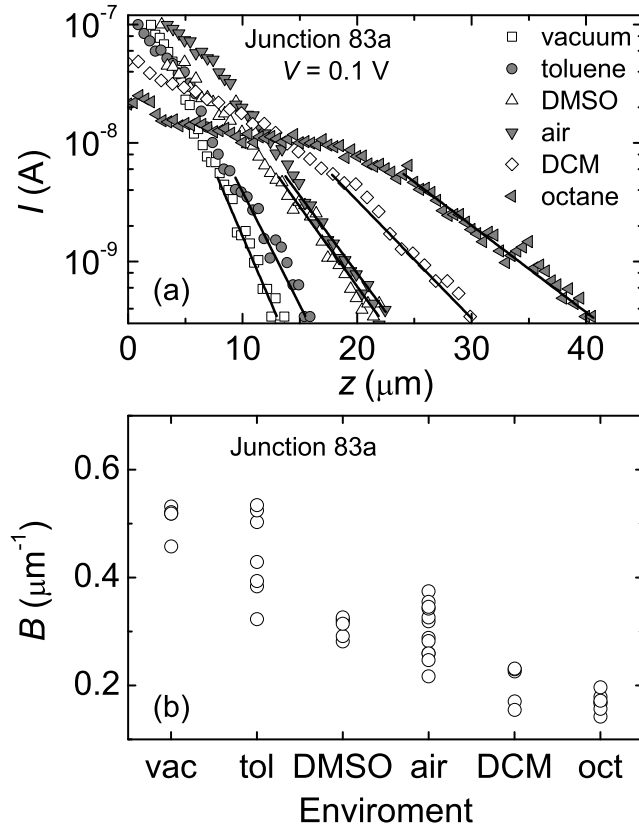


Figure 4.4: Tunnelling regime: (a) Raw data for the current versus the vertical displacement of the push-rod  $z$  for a single gold junction (83a) in different environments. The curves are shifted horizontally for clarity, and the zero in  $z$  has been arbitrarily chosen. The solid lines are obtained from fits of  $I(z)$  to an exponential law. (b) Results for the slope  $B$  from fitting an exponential law to several sets of curves similar to that shown in part (a).

tunneling through liquids. Reduced effective tunnelling barrier heights  $\phi$  have been consistently observed in STM experiments performed in aqueous environments. Schmickler and Henderson [61] consider a model system consisting of a dielectric continuum representing the water in between the metal tip and the surface. The tunnelling electrons interact with the electronic polarizability of water reducing the barrier height by about 1 eV. Saas *et al.* [62] proposed electron tunnelling via intermediate states, which is also reducing the apparent barrier height. The intermediate states are built of hydrated electrons. Another proposal given by Boussaad *et al.* [63] explains the fluctuations in the tunnelling current in metal-water-metal junctions with a localized state model leading to

two-level fluctuations. In contrast Lindsay and co-workers [64] considered a resonant tunnelling model through several water molecules in a tunnelling pathway. Another interesting effect observed with an STM is the layering effect of water molecules leading to oscillations in the tunnelling barrier height [65]. The oscillation period was close to the calculated distance of water molecules in the Helmholtz layer of the solid/liquid interface.

In spite of these attempts a consistent and detailed model providing a quantitative account for a decrease in the tunnelling barrier height is still lacking. We point out that the observed decrease in  $B$  does not show a simple correlation with the dielectric constant (whether static or optical) of the medium in between the electrodes [66, 67]. We rather suspect that mechanical effects linked to the discrete nature of the dielectric medium within the electrodes gap account for the variation of  $B$  with the environment in the low current region. This subject is discussed in the next section.

#### 4.3.1 Tunneling through alkanes and alkanethiols

The discrete nature of the liquid plays a significant role for the tunneling current. A remarkable effect can be seen in Fig. 4.4 (a) where a striking change of slope appears in the octane curve. This behaviour could be reliably observed for all curves measured in octane after a number of open-close cycles ( $>30$ ) allowing the junction to stabilize. Fig. 4.6 shows a comparison of tunneling current  $I$  versus  $z$  in air and in octane for the same junction. The octane curves clearly exhibit a change in the slope at higher current. A decrease in the slope corresponds to a lower-

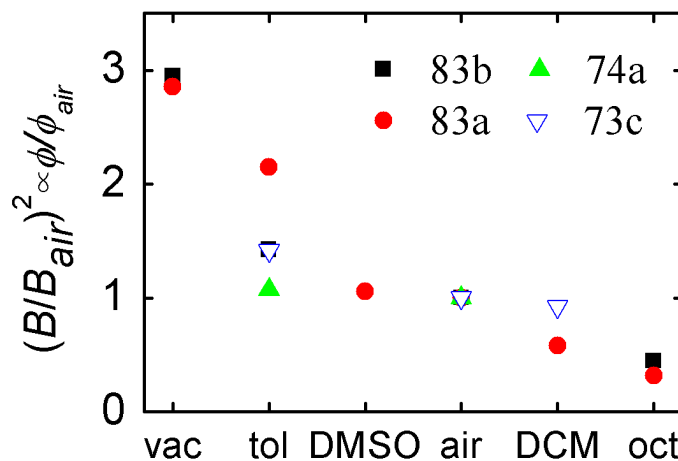


Figure 4.5: The ratio of the mean value of  $B$  in different environments with respect to that of air for four different samples.



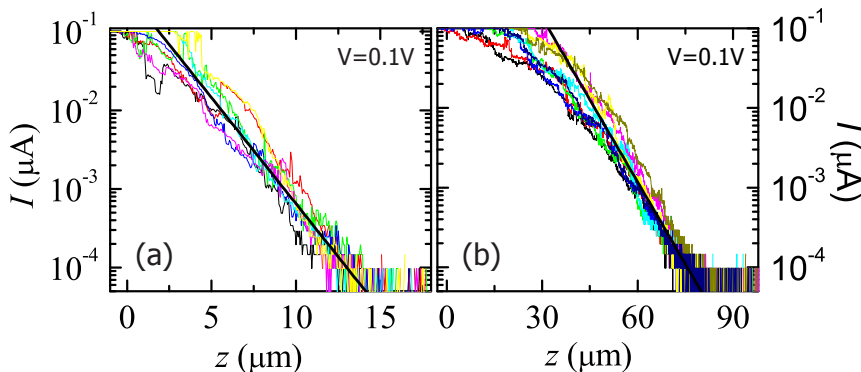


Figure 4.6: Raw data with the fitted curves for the current versus the vertical displacement of the push-rod  $z$  measured in (a) air and (b) in octane. The octane curves show a clear change of the slope.

ing of the apparent barrier height. This is likely caused by the discrete (molecular) nature of the liquid and its behavior in confined geometries [68, 69]. STM investigations have shown that *n*-alkane chains tend to self-organize parallel to a Au(111) surface [70]. A layering of the octane molecules at short inter-electrodes separations can explain the reduced slope of  $\ln(I)$  versus  $z$  at small gap sizes: for a given vertical displacement  $z$ , the effective shortening of the gap becomes smaller due to the mechanical resistance opposed by the layered octane molecules in between the Au electrodes, deforming the Au extremities. Consequently, a more gentle current increase with vertical displacement results. To a lesser extent, the DCM curve ( $\diamond$ ) also exhibits a similar saturating behavior, see Fig. 4.4 (a).

We observed a similar change of slope while measuring in decanethiol ( $C_{10}H_{21}SH$ ) and hexadecanethiol ( $C_{16}H_{33}SH$ ) both used as a 0.1 mM solution in toluene. Two sets of consecutive curves are shown in Fig. 4.7, measured with the same junction.

The effect is very pronounced in hexadecanethiol, see Fig. 4.7 (b). Also the curves recorded in decanethiol shown in Fig. 4.7 (a) exhibit two different slopes, but in a less striking manner than in (b). In contrast to alkanes, alkanethiols form a self-assembled monolayer on gold with a covalent bond of the sulfur to the gold. The effect on the current when approaching the electrodes is expected to be stronger for a monolayer of thiols than for alkanes, as the latter are not bond to the surface. The remarkable change of the slope in Fig. 4.7 (b) is a strong indication of the molecular order. While approaching the two electrodes of the break junction, the two monolayers of decanethiols and maybe also the Au extremities deform. The alkanethiols may even interlock, as indicated in Fig. 4.8. Furthermore, the molecules act as a mechanical resistance

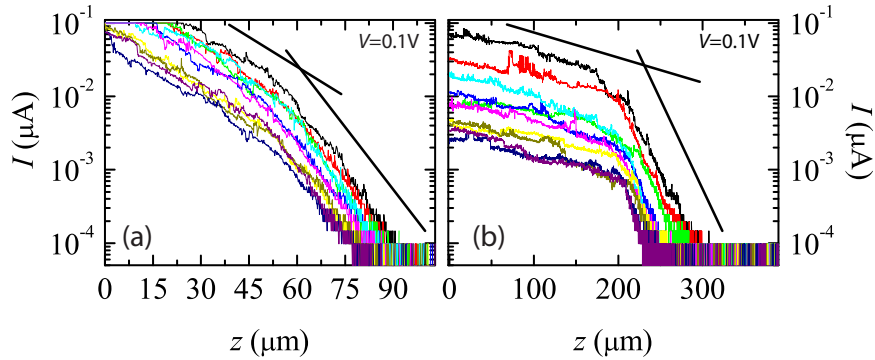


Figure 4.7:  $I$  versus  $z$  curves in (a) decanethiol and (b) hexadecanethiol, measured with the same junction. The 10 curves are recorded one after the other without waiting time in between. The solid lines are guides to the eye.

opposing a further compression, as already discussed in connection with alkanes. This is reflected in the slope change in Fig. 4.7 (a). If two monolayers of hexadecanethiols are pressed against each other, the deformation of the monolayer will be smaller and the mechanical resistance opposed by the layered molecules higher, due to the higher intermolecular interaction of hexadecanethiols compared with decanethiols. Therefore, the change in the slope in Fig. 4.7 (b) is more prominent than in Fig. 4.7 (a).

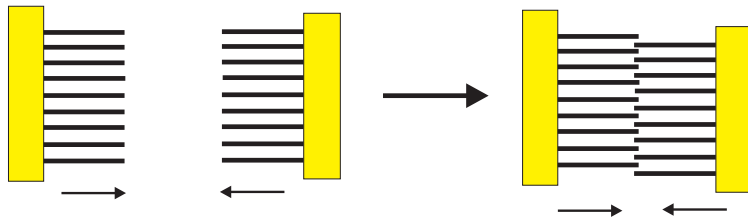


Figure 4.8: Schematics of alkanethiols on two gold electrodes facing each other. While approaching the two electrodes, the monolayers are compressed.

## 4.4 Conclusion

The micro-fabricated break junctions can be operated in a liquid environment opening interesting perspectives to study single-molecule devices in a chemically active environment. We observed that the solvent significantly affects the tunneling regime and obtained good evidence that the confinement of the liquid can lead to molecular layering effects within the gap. We emphasize that the strain limitation of the substrate causes significant variations in the mechanical reduction factor. Despite this difficulty, we could observe a systematic and reproducible trend in the variation of the tunneling barrier height with different solvents.



## Chapter 5

# Resonant tunneling through a C<sub>60</sub> molecular junction in liquid environment

### 5.1 Introduction

Since the discovery of C<sub>60</sub> in 1985 [71], Buckminsterfullerenes and in particular C<sub>60</sub> and its derivatives have attracted much attention [72] and, due to their particular electronic properties, represent ideal model systems for molecular electronics [11, 73, 74]. Special effort has been directed to molecular level spectroscopy of C<sub>60</sub>, and in particular to effects that result in shifting and splitting the electronic levels of excited and ionized molecules, such as the Jahn-Teller distortion [75, 76].

We performed transport measurements on 3 different derivatives of C<sub>60</sub> shown in Fig. 5.1. Only compound **1** showed a convincing signal. Compound **2** is not fixed on the gold surface due to a missing anchor group and therefore freely mobile. In the latter case we observed rarely a signal from the molecule in the current vs. distance curves. The same holds for **3**, as the methylsulfide end group cannot provide a bond to the gold surface. In the following only transport measurements of the thiolated compound **1** are presented and discussed.

The two probe configuration sketched in Fig. 5.2 is provided by the tips of a break junction. The single functional group serves as an anchor and, in the case where a single molecule junction is realized, permits to control the coupling of the C<sub>60</sub> to a Au electrode by mechanically adjusting the inter-electrode spacing  $d$ . By performing transport measurements in two distinct solvents, dimethylsulfoxide (DMSO) and toluene, we could observe the strong influence of the environment on the molecular junctions.

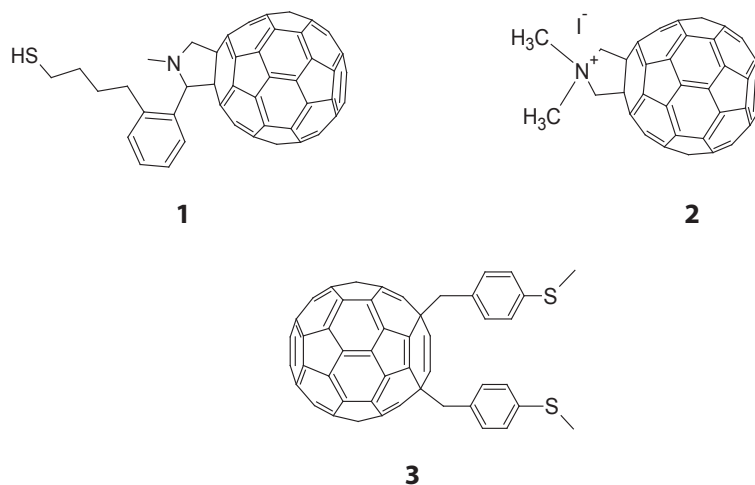


Figure 5.1: The three  $C_{60}$  derivatives tested in the break junction. (a) Thiol functionalized  $C_{60}$ , (b) pyrrolidinium functionalized  $C_{60}$  and (c) *bis*-methylsulfide functionalized  $C_{60}$ . Synthesis by F. Diederich *et al.*

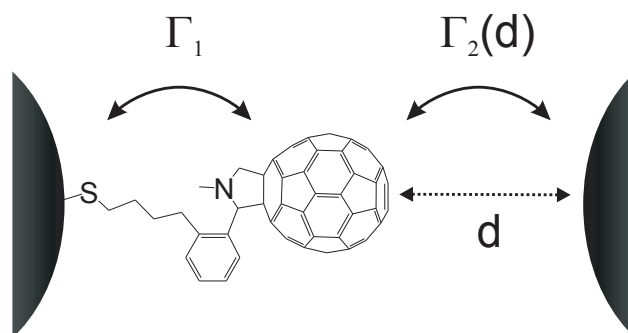


Figure 5.2: Schematic representation of a break junction with a thiolated  $C_{60}$  molecule anchored to the left electrode. The distance  $d$  between the molecule and the right electrode can be adjusted by opening and closing the junction.

## 5.2 Experimental part and measurements

The synthesis of the fullerene derivatives was carried out by Diederich *et al.* following well-established chemistry [77]. A thiolated C4 linker ensured that the C<sub>60</sub> molecule would bind to the gold electrodes.

We first characterized the gold junctions via measurements of the conductance  $G(d)$  versus distance  $d$  in air and in the solvents used subsequently for the C<sub>60</sub> molecules, toluene and dimethyl sulfoxide (DMSO). Several sets of consecutive open-close cycles were recorded, with  $G$  ranging typically between  $0.001 G_0$  and a few  $G_0$ , where  $G_0 = 2e^2/h$  is the conductance quantum. To investigate the transport through C<sub>60</sub> molecules, a 0.1 mM C<sub>60</sub> solution was added to the liquid cell while the junction was kept close. The junction was then opened widely ( $\approx 5$  nm) to favor the self-assembly of the molecules. We also added molecules while keeping the junction open but no significant differences in the transport measurements were observed. Sets of 10 – 30  $G(d)$  curves were recorded at time intervals of 30 – 45 min. During these cycles, the junction was never fully closed, keeping its conductance below  $0.1 G_0$  in order to limit mechanical rearrangements of the Au tips.  $G(d)$  obtained while closing the junction are shown in Fig. 5.3 for DMSO (a) and toluene (b) at a bias voltage of  $V_b = 0.2$  V. Two detailed measurement sequences are presented in Appendix A, one in DMSO and one in toluene. They show the development of the peak in the conductance curves with time.

The open symbol curves in Fig. 5.3 show measurements in the pure solvent. The solid curves are five successive raw measurements performed after adding the C<sub>60</sub> solution to the junction. We also attempted to measure current-voltage ( $I - V$ ) characteristics. But these curves were not reproducible displaying rather large uncontrolled mechanical hysteresis, which we assign to the dynamics of the liquid environment and the relatively weak tethering of the C<sub>60</sub> with one single linker group only. While the measurements of  $G(d)$  in the pure solvents show a clean exponential behavior (see Chapter 2), the curves for the C<sub>60</sub> modified junctions exhibit a more complex structure. Until today, the occurrence of a plateau in the  $G(d)$  has been taken as the signature for the ‘locking-in’ of a molecule [37]. We observe a plateau in about 50 % of the measured closing cycles. In addition to this observation, a pronounced peak can appear (arrow in Fig. 5.3). Though the peak appears less frequently, reproducible measurements (visible in each closing curve within a cycle of 10 curves at least) could be measured for both C<sub>60</sub> in DMSO and toluene. In DMSO, the peak corresponds to a conductance maximum of  $\simeq 0.012 G_0$  and is followed by a plateau-like feature with a slow conductance increase. When further closing the junction the conductance rises more rapidly, although less sharply than in the pure solvent. The shape of the conductance curves in toluene (Fig. 5.3b) is very different, showing more noise and a fully developed peak. After a small pre-peak (not present in all curves), the conductance rises to a maximum value

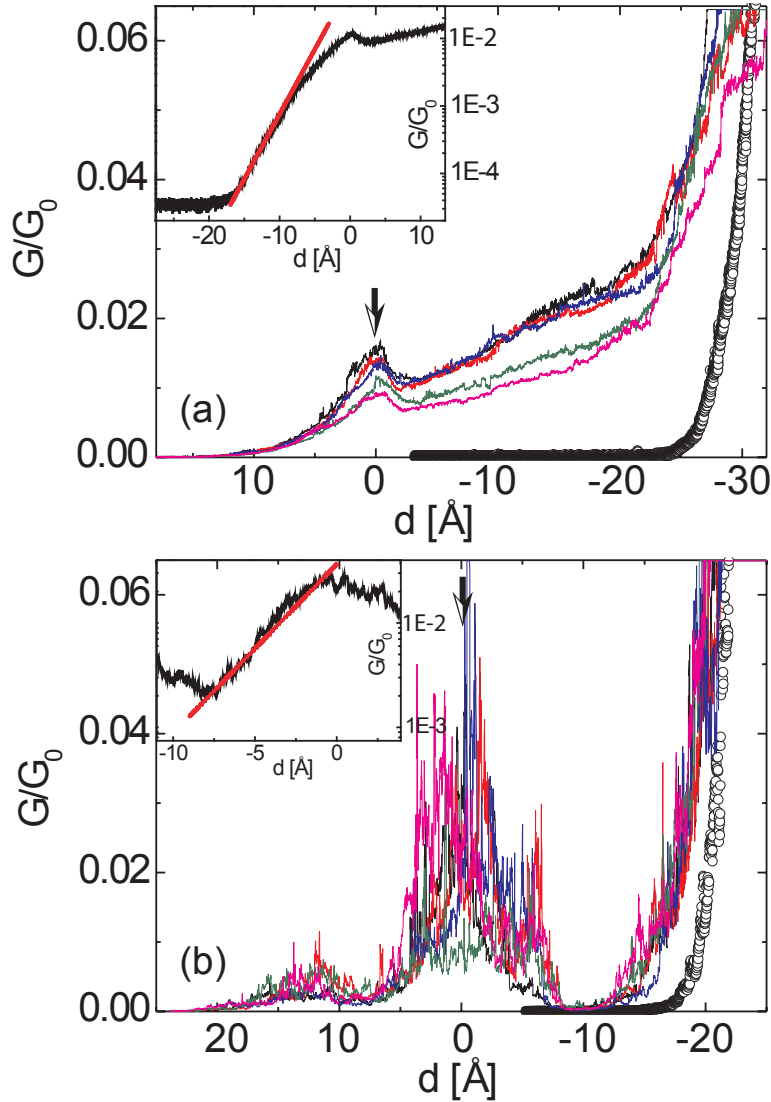


Figure 5.3: Conductance  $G$  versus distance  $d$  curves in DMSO (a) and toluene (b) measured at a bias voltage of 0.2 V while closing the junction. The open symbol curves were measured in the pure solvent. The solid lines are raw data for five successive measurements after adding the  $C_{60}$  solution. The insets show averaged (over 10 curves) conductance data in a log-lin representation. The value for the inverse decay rate  $\kappa$  was obtained from a linear fit (dashed lines) to  $G/G_0$  in the low conductance regime:  $\kappa_{DMSO} = 0.43 \text{\AA}^{-1}$  and  $\kappa_{toluene} = 0.37 \text{\AA}^{-1}$ . Note, that the zero in the distance scale  $d$  was chosen to match with the position of the peak.



of  $\approx 0.025 G_0$  at the peak and decays again to a very low conductance. While further closing the junction the conductance increases sharply, with a slope similar to that of the conductance in the pure solvent. The environment in which the junction is studied plays clearly an important role here. We note in particular that DMSO is a rather poor solvent for neutral fullerenes, whereas toluene is a good solvent (see e.g. [78]).

As explained in Chapter 2 and 4 we calibrated each junction by measuring the tunneling conductance between the two Au electrodes in the pure solvent. Let us denote the gap distance between the two Au electrodes by  $d_{gap}$ . It can be expressed as  $d_{gap} = az$ , where  $z$  denotes the vertical displacement of the push-rod and  $a$  the attenuation factor, which is discussed in Chapter 2. The factor  $a$  needs to be calibrated for each junction. The tunneling conductance  $G(d)$  measured in pure solvent was fitted according to the expression  $G \propto \exp[-\kappa az]$  with  $\kappa = 2\sqrt{2m\phi}/\hbar$ , where  $\phi$  (and  $\kappa$ ) represents the height of a square tunneling barrier of width  $d$  and  $m$  is the electron mass. The fits were adjusted by tuning  $a$  in order to obtain values for  $\phi$  in agreement with Chapter 4 in which the apparent workfunctions in different solvents were calibrated with respect to measurements in vacuum. The reference inverse decay lengths  $\kappa$ , valid for the pure solvents, are  $\kappa_{toluene} = 0.85 \text{ \AA}^{-1}$  and  $\kappa_{DMSO} = 0.63 \text{ \AA}^{-1}$ . This procedure provides the attenuation factor  $a$  for each junction measured.

### 5.3 Discussion

The particularity of our system lies in the single anchor group used to tether the molecule within the break junction. This configuration makes it possible to tune the coupling of the molecule to the electrode: while one tunneling rate ( $\Gamma_1/\hbar$ ) is fixed, the second ( $\Gamma_2/\hbar$ ) varies exponentially with the gap between the electrode (electrode to the right in Fig. 5.2) and the C<sub>60</sub> molecule. The metal–molecule–metal junction forms a double-barrier junction. In this picture, the observed conductance peaks can be explained within a coherent resonant tunneling model, provided that one of the energy levels of the molecule lies not too far away from the Fermi level of the electrodes. If the electrodes are far apart from the molecule, there is no coupling and the energy level is well defined. The coupling to the contacts broadens the discrete energy level (Fig. 5.4) into a continuous density of states which is given by [79]

$$D_\varepsilon(E) = \frac{\Gamma/2\pi}{(\varepsilon)^2 + (\Gamma/2)^2}, \quad (5.1)$$

with  $\Gamma = \Gamma_1 + \Gamma_2$  and  $\varepsilon = E_m - E_F$ .  $E_m$  is the molecular level energy and  $E_F$  the Fermi energy of the electrodes. Taking the broadening into account, we can express the current as

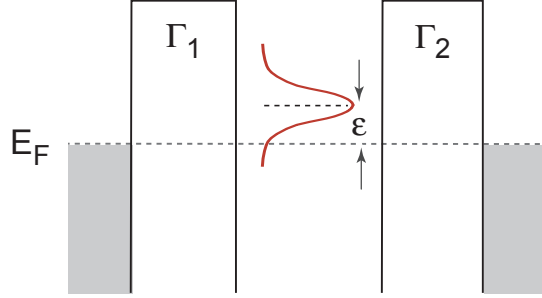


Figure 5.4: Schematics of the energetics of a double-barrier junction with a single molecular level positioned at  $\varepsilon$  relative to the Fermi energy  $E_F$  of the metallic reservoirs. The coupling to the electrodes broadens the energy level according to a Lorentzian function with width  $\Gamma = \Gamma_1 + \Gamma_2$ .

$$I = \frac{q}{h} \int_{-\infty}^{+\infty} dE D_\varepsilon(E) \frac{\Gamma_1 \Gamma_2}{\Gamma_1 + \Gamma_2} [f_1(\varepsilon) - f_2(\varepsilon)] \quad (5.2)$$

It can be written as

$$I = \frac{q}{h} \int_{-\infty}^{+\infty} dE T(E) [f_1(\varepsilon) - f_2(\varepsilon)], \quad (5.3)$$

where the transmission  $T$  is defined as

$$T(E) = 2\pi D_\varepsilon(E) \frac{\Gamma_1 \Gamma_2}{\Gamma_1 + \Gamma_2} = \frac{\Gamma_1 \Gamma_2}{(\varepsilon^2 + ((\Gamma_1 + \Gamma_2)/2)^2)}. \quad (5.4)$$

At low temperature we can rewrite Eq. 5.3 as

$$I = \frac{q}{h} \int_{-\mu}^{+\mu} dE T(E) \quad (5.5)$$

with  $+\mu = +eV/2$  and  $-\mu = -eV/2$ . In the linear regime ( $eV \rightarrow 0$ ), the expression for the conductance  $G$  (Breit-Wigner) is then

$$G = \frac{2e^2}{h} \frac{\Gamma_1 \cdot \Gamma_2}{\varepsilon^2 + (\Gamma_1 + \Gamma_2)^2/4}. \quad (5.6)$$

Resonant tunneling through a single level  $\varepsilon$  results in a peak in the linear conductance  $G$  when the level aligns with the Fermi level  $E_F$  of the leads, i.e. at  $\varepsilon = 0$ . The occurrence of a peak in  $G(\varepsilon)$  is a well known fact [80]. However, a peak can also arise in  $G(\Gamma_2)$ , even if  $\varepsilon \neq 0$ .

In our geometry,  $\Gamma_1$  is fixed and defined by the molecular tether holding the molecule to the left electrode (Fig. 5.2).  $\Gamma_2$  depends exponentially on the distance  $d$  between the C<sub>60</sub> molecule and the right electrode with  $\kappa$

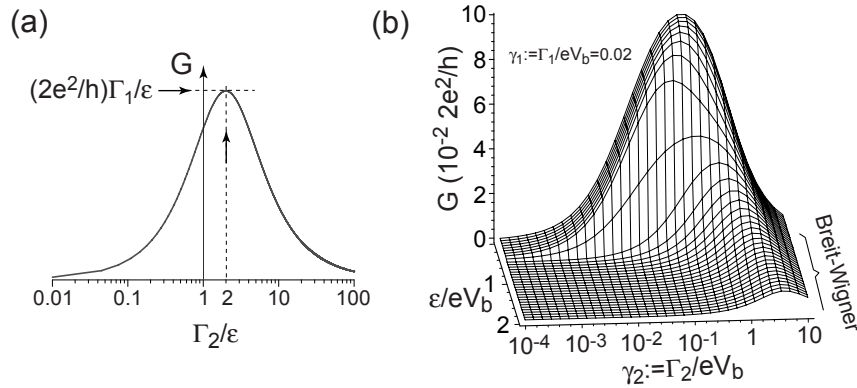


Figure 5.5: (a) Linear-response conductance  $G$  as a function of  $\Gamma_2$  for the double-barrier shown in 5.4, assuming coherent tunneling and  $\Gamma_1 \ll \varepsilon$ . (b) Same as (a), but taking into account the finite bias voltage  $V_b \gg k_b T$ . This illustration has been obtained for a specific value of  $\Gamma_1 = 0.02 V_b$ . A pronounced crossover is observed at  $\varepsilon = eV_b/2$ .

being the inverse decay length, i.e.  $\Gamma_2(d) = \Gamma_2^* \cdot e^{-\kappa d}$ .  $G(\Gamma_2)$  in Eq. (5.6) as a function of  $\Gamma_2$  has a maximum  $G_{max}$  at  $\Gamma_2^* = \sqrt{4\varepsilon^2 + \Gamma_1^2}$ . If  $\varepsilon \ll \Gamma_1$ , we would have  $\Gamma_2^* = \Gamma_1$ , and consequently a peak conductance of  $G_{max} \simeq G_0$ . In the experiment, the peak conductance is however much smaller than  $G_0$ , so that  $\Gamma_1 \ll \varepsilon$ . It follows then that  $\Gamma_2^* \simeq 2\varepsilon$  and  $G_{max} = G_0 \cdot \Gamma_1/\varepsilon$ . A respective plot in this limit ( $\Gamma_1 \ll \varepsilon$ ) is shown in Fig. 5.5 (a). Note that we define  $\varepsilon \geq 0$ , but the sign of  $\varepsilon$  is not determined, i.e. a sign change in  $\varepsilon$  does not affect the discussion.

Using the Breit-Wigner equation, we can obtain the ratio  $\Gamma_1/\varepsilon$  from the measured peak height without fitting. The measurements yield  $\Gamma_1/\varepsilon \simeq 1.1 \cdot 10^{-2}$  in DMSO and  $\Gamma_1/\varepsilon \simeq 2.7 \cdot 10^{-2}$  in toluene, more than twice the DMSO value. Because we expect  $\Gamma_1$  to be the same for both solvents (after all it is the same linker), this suggests that the level is lying closer to the Fermi level of the electrodes in toluene as compared to DMSO.

That we can measure directly the ratio  $\Gamma_1/\varepsilon$  is a very nice fact. But we would like to obtain both  $\varepsilon$  and  $\Gamma_1$ . This is at first sight not possible, because Eq. (5.6) is scale-invariant. Changing  $\Gamma_1$ ,  $\Gamma_2$ , and  $\varepsilon$  by the same factor leaves the curve invariant. To our rescue, we emphasize that we did not measure the linear-response conductance, but  $G$  at a bias of  $eV_b = 0.2 \text{ eV}$ , much larger than  $k_B T$  at room temperature. The finite bias introduces an energy scale which allows us the narrowing down of the range of possible values considerably. Integrating Eq. (5.5) over the

bias window, given by the applied voltage  $V_b$ , yields:

$$G = \frac{4e^2}{h} \frac{\gamma_1 \gamma_2(d)}{\gamma_1 + \gamma_2(d)} \left[ \arctan \left( \frac{1 - 2\tilde{\varepsilon}}{\gamma_1 + \gamma_2(d)} \right) + \arctan \left( \frac{1 + 2\tilde{\varepsilon}}{\gamma_1 + \gamma_2(d)} \right) \right] \quad (5.7)$$

All parameters are now scaled to  $V_b$ , i.e.  $\gamma_i = \Gamma_i/eV_b$ ,  $\gamma_2(d) = \gamma_2^* \cdot e^{-\kappa d}$ , and  $\tilde{\varepsilon} = \varepsilon/eV_b$ . There are two regimes: a)  $\varepsilon \lesssim eV_b/2$  and b)  $\varepsilon \gg eV_b/2$ , the latter corresponds to the Breit-Wigner equation. In both cases a peak develops in  $G(\gamma_2)$ , but there is a pronounced crossover, which sets in sharply at  $\tilde{\varepsilon} := \varepsilon/eV_b = 0.5$ . This crossover is shown in Fig. 5.5 (b) for a selected value of  $\gamma_1 = 0.02$ .

In the following, we will try to fit our measurements to Eq. (5.7) in both the low and large  $\varepsilon$  limit. There are four fitting parameters:  $\varepsilon$ ,  $\Gamma_1$ ,  $\Gamma_2^*$ , and  $\kappa$ . Note that we always use the ansatz  $\Gamma_2 = \Gamma_2^* e^{-\kappa d}$  and that we define the zero of the distance axis  $d$  to match with the peak position in the measurement. This is possible as we have no means to determine the ‘true’ zero, i.e. the point of contact of the right electrode with the C<sub>60</sub> molecule.

In the first step, we obtain  $\kappa$  by focussing on large  $d$ , where the junction is widely open and the conductance well below the conductance at the peak. In this simple tunneling regime,  $G \propto \Gamma_2 \propto e^{-\kappa d}$ . From fits to the averaged conductance curves of the C<sub>60</sub>-modified junctions (Fig. 5.3 insets), we extract the inverse decay lengths  $\kappa_{DMSO} = 0.43 \pm 0.01 \text{ \AA}^{-1}$  and  $\kappa_{toluene} = 0.37 \pm 0.05 \text{ \AA}^{-1}$ . We emphasize that the value obtained for DMSO is more reliable than the one for toluene, since the fit could be performed over a more extended range of conductance. This is due to the presence of a lower conductance peak in toluene (see Fig. 5.3 (b)). The inverse decay lengths  $\kappa$  are slightly suppressed as compared to the values measured in the solvent alone (Chapter 4).

We next compare our data to conductance curves calculated for the limiting case  $\varepsilon = 0$ . We fix the  $\kappa$  values to the ones determined for large  $d$  and try to obtain a good match with the experiment by tuning both  $\Gamma_1$  and  $\Gamma_2^*$ . The dashed lines in Fig. 5.6 show curves for  $\Gamma_{1,DMSO} = 0.92 \text{ meV}$  and  $\Gamma_{2,DMSO}^* = 2.7 \text{ meV}$ , and  $\Gamma_{1,toluene} = 2.2 \text{ meV}$ ,  $\Gamma_{2,toluene}^* = 3.9 \text{ meV}$ . In both cases, the adjusted curves present a substantially broader peak than the data, showing that the limit  $\varepsilon = 0$  is inappropriate.

We now relax the condition  $\varepsilon = 0$  and try to find the *smallest* possible  $\varepsilon$  for which a good match between the calculated and measured curve is obtained, again using the  $\kappa$  values determined for a large  $d$ . We obtain  $\varepsilon_{DMSO} \simeq 0.20 \text{ eV}$ ,  $\Gamma_{1,DMSO} \simeq 4.3 \text{ meV}$ ,  $\Gamma_{2,DMSO}^* \simeq 0.35 \text{ eV}$ , and  $\varepsilon_{toluene} \simeq 0.12 \text{ eV}$ ,  $\Gamma_{1,toluene} \simeq 5.5 \text{ meV}$ ,  $\Gamma_{2,toluene}^* \simeq 74 \text{ meV}$ . Care has to be taken at this point, because  $\varepsilon_{toluene} \simeq 0.12 \text{ eV}$  is very close to the transition region between the Breit-Wigner and the  $\varepsilon = 0$  case where the theoretical  $G(d)$  curves are quite sensitive to the temperature. When taking the finite temperature into account,  $\varepsilon_{toluene}$  slightly increases.

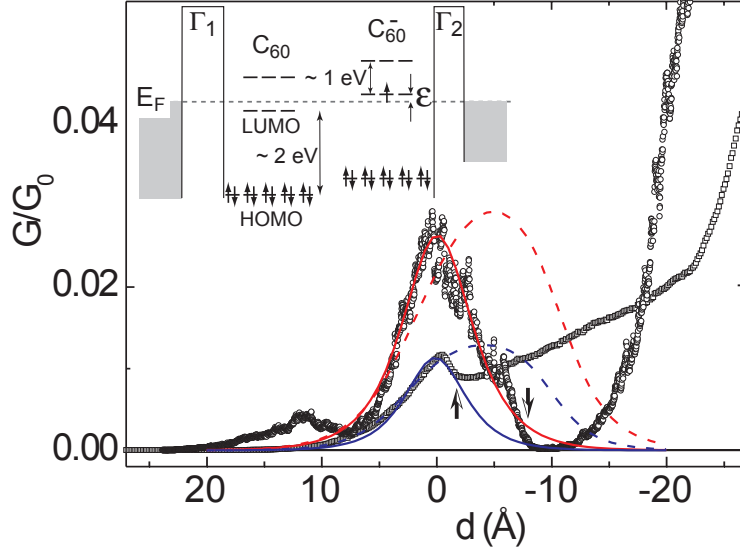


Figure 5.6: Averaged conductance versus distance curves for DMSO ( $\square$ ) and toluene ( $\circ$ ). The solid lines are fits to the data using Eq. (5.1) with  $\Gamma_1/\varepsilon=1.1 \cdot 10^{-2}$  ( $2.7 \cdot 10^{-2}$ ) and  $\kappa = 0.43 \text{\AA}^{-1}$  ( $0.37 \text{\AA}^{-1}$ ) for DMSO and (toluene). The dashed lines were calculated from Eq. (5.2) in the limit  $\varepsilon = 0$ : 0.92 meV ( $\Gamma_1 = 2.2$  meV), 2.7 meV ( $\Gamma_2^* = 3.9$  meV), and  $0.43 \text{\AA}^{-1}$  ( $\kappa = 0.37 \text{\AA}^{-1}$ ) for DMSO and (toluene). *Inset*: Schematic energy diagram of the metal-molecule-metal junction showing the energy level of  $C_{60}$  and  $C_{60}^-$ . Due to its large electronegativity,  $C_{60}$  tends to gain charge from a nearby metallic surface as illustrated by the position of its LUMO level, lying below the Fermi energy of the Au electrodes.

This is due to the level broadening which results in a higher overlap between the electrode and the molecular level. In this case, a higher  $\varepsilon$  results in the same conductance. In this sense  $\varepsilon \gtrsim 0.15 - 0.2$  eV is a good approximation for both DMSO and toluene.

If we allow for larger values of  $\varepsilon$  we cross over to the Breit-Wigner equation. In this scale-invariant limit, we obtain convincing fits for both DMSO and toluene with the parameters  $\Gamma_1/\varepsilon = 0.011$  (DMSO) and 0.027 (toluene), and  $\Gamma_2^*/\varepsilon = 2$  as required (solid lines in Fig. 5.6). Hence, at this stage we can say with confidence that  $\varepsilon \gtrsim 0.15 - 0.2$  eV for both DMSO and toluene.

As emphasized before, the Breit-Wigner formula cannot provide an upper bound for  $\varepsilon$ . However, we can – on a physical ground – provide an upper bound on  $\Gamma_2$  and therefore also on  $\varepsilon$ . The latter is obtained through the relation  $\Gamma_2^* = 2\varepsilon$ . The peak in  $G(\Gamma_2)$  appears at relatively large  $\Gamma_2$  values, but  $\Gamma_2$  cannot grow to too high values, because otherwise

higher molecular states of the C<sub>60</sub> molecule will strongly hybridize with the states in the Au electrode and the model will break down. Moreover, a large  $\Gamma_2$  at short distances corresponds to a large binding force of order  $\kappa\Gamma_2$  between the molecule and the Au electrode. In fact, we think that the crossover from the peak to the plateau in DMSO is determined by this consideration. Furthermore, the fully developed peak in toluene suggests that  $\Gamma_2$  at the position of the peak ( $\Gamma_2^*$ ) is smaller in toluene than in DMSO.

In order to fix the upper bound of  $\Gamma_2$ , we need to discuss the typical energy scales of the orbitals in C<sub>60</sub>. We do not take into account the modifications in the orbitals induced by the anchor group attached to C<sub>60</sub>. In the inset of Fig. 5.6 we show the energy levels of C<sub>60</sub> and C<sub>60</sub><sup>-</sup> (adapted from Green *et al.* [75]). The HOMO-LUMO gap of C<sub>60</sub> determined in solution is around 2.3 eV [81] whereas local density approximation calculations provide a value of 1.9 eV for the free C<sub>60</sub> molecule (see e.g. [72] and refs. therein). Experiments on C<sub>60</sub> monolayers assembled on metallic surfaces showed values ranging from 1.5 eV to 3.0 eV [82, 83, 84, 85].

Due to its high electronegativity, a C<sub>60</sub> molecule in contact with a metal tends to gain charge from the metal. The ionization potential of Au is 5.3 eV and the electron affinity of C<sub>60</sub> equals 2.8 eV. The latter includes the Coulomb energy of the singly charged C<sub>60</sub> amounting to  $\approx 3$  eV. If we assume that the Coulomb energy is strongly screened in the gap between the Au electrodes, C<sub>60</sub>  $\rightarrow$  C<sub>60</sub><sup>-</sup> is favorable. Photoemission studies of C<sub>60</sub> on a Au surface yield values for the electron charge on C<sub>60</sub> of 0.8 [86] and 1.0 [87]. Hence, it is very likely that C<sub>60</sub> is singly charged also in our work. On acquiring an electron the threefold degenerate LUMO state of C<sub>60</sub> splits by a very small amount of 8 meV (not shown and also not resolvable in our experiment) and the chemical potential  $E_F$  is expected to align closely with this orbital (dashed line). In fact,  $E_F$  may lie above ( $\varepsilon > 0$ ) or below ( $\varepsilon < 0$ ), depending on the exact charge state.

Taking the HOMO-LUMO gap of the C<sub>60</sub> and the C<sub>60</sub> anion as the proper energy scales,  $\Gamma_2 \lesssim 1 \dots 2.3$  eV to avoid hybridization with higher lying orbitals. If we impose that this condition occurs in DMSO at the transition from the peak to the observed plateau at  $d = -2$  Å (see arrow in Fig. 5.6), we obtain  $\varepsilon_{DMSO} < 0.2 \dots 0.5$  eV. Together with the previous consideration,  $\varepsilon$  is determined quite accurately to  $0.2 < \varepsilon_{DMSO} < 0.5$  eV. Similarly, if we pretend to describe the full peak in toluene up to  $d = -7$  Å (arrow), we obtain  $\varepsilon_{toluene} \lesssim 0.04 \dots 0.09$  eV. These rather small values for  $\varepsilon$  are inconsistent with the previous consideration. In order to obtain an upper bound for  $\varepsilon_{toluene}$  of at least 0.2 eV, one would have to set the cut-off to as large a value as  $\Gamma_2 \leq 5$  eV. This disagreement shows that the full decay of  $G(d)$  in toluene to approximately zero conductance beyond the peak must have another origin. This will be addressed in the following.

We have assumed here that we are allowed to use the resonant tunneling model with an unperturbed level beyond the peak. However, a full understanding of the small  $d$  regime would require the understanding of local rearrangement effects taking place when the electrodes and the molecules are reaching mechanical contact. In the case of toluene we observe that the conductance drops to a negligibly small value after the peak and then shows a pronounced increase, similarly to the behavior of the junction in the pure solvent (Fig. 5.3 (b)). We can presume that, upon closing of the junction to small values of  $d$ , the molecules are pushed away from the inter-electrode space, resulting in conductance properties dominated by Au-Au tunneling. The shoulder observed in the case of DMSO (Fig. 5.3 (a)) lets envision a different scenario in which the molecules remain within the junction and therefore continue to substantially affect the conductance of the junction at very short inter-electrode separations. Additionally, large conductance fluctuations can be observed in toluene (see Fig. 5.3 (b)) while the curves are much smoother in DMSO. We attribute these differences to the solubility of the fullerene derivate in the solvent considered. Whereas toluene is a good solvent, the fullerenes tend to aggregate with time when suspended in DMSO. In our view, the large conductance fluctuations observed in toluene reflect the tendency of the fullerene molecules to be re-solved if the cavity is getting to narrow. In contrast, the molecules rather stay within the junction if DMSO is used, due to the lower solvation energy. Whether a single molecule picture really holds in such a system is an important question. The very good match between theory and experiment supports the single molecule approach. The analysis provides more than a qualitative agreement with the data and allows the extraction of narrowed range estimates for the LUMO position and the tunneling rate  $\Gamma_1$  of the molecular bridge between the Au electrode and the  $C_{60}$  molecule. The results are:  $\varepsilon = 0.2 \dots 0.5$  eV, and  $\Gamma_1/\varepsilon = 1.1 \dots 2.7 \cdot 10^{-2}$ .

We have also checked that charge transfer (within a self-consistent mean field theory [88]) does not significantly change the shape of the conductance versus distance curves. Such effects would mostly result in a slight scaling of the parameters  $\varepsilon$ ,  $\Gamma_1$  and  $\Gamma_2^*$ .

The presence of a much lower peak in some raw conductance curves in toluene (about  $12 \text{ \AA}$  prior to the main peak, Fig. 5.3 (b)) might be a signature for a weaker tunneling process involving  $C_{60}$  molecules on both electrodes. If running experiments confirm this feature, an interpretation in terms of a triple-barrier system could further support this approach.

## 5.4 Conclusion

We have performed transport measurements through C<sub>60</sub> molecules tethered by a single anchor group in Au break junctions operated in a liquid environment. The signature of the presence of the molecules within the junction appeared as a peak in conductance versus distance curves. The shape of this peak was strongly influenced by the solvent in which the junction was operated, thereby showing the importance of a proper environmental control in nanoscale junctions.

The data can be understood in a resonant tunneling picture through a single level located close to the Fermi energy  $E_F$ . The particular geometry of the experiment combined with the environmental control allowed us to provide numbers for the electronic tunneling rates between a gold electrode and a fullerene derivative. By systematically varying the linker group, our approach will allow to better understand the electronic coupling between molecules and electrodes in molecular devices. Moreover, gating will allow the resonant level to be moved even closer to the Fermi level. An increase of the conductance up to the quantum conductance value can then be envisaged.



## Chapter 6

# Transport measurements through TTF derivatives in liquid environment

### 6.1 Introduction

Tetrathiafulvalene (TTF) and its derivatives have been extensively studied for more than 25 years and are well known as versatile strong  $\pi$ -electron donors in material chemistry. The compound can be oxidized reversibly to TTF<sup>+</sup> and TTF<sup>2+</sup>, as indicated in Fig. 6.1. The oxidation to the cation radical **2** and the di-cation species **3** occurs sequentially and reversibly (the half wave oxidation potentials for unsubstituted TTF are  $E_1^{1/2}=+0.34$  V and  $E_2^{1/2}=0.78$  V, vs. Ag/AgCl in acetonitrile [89]). In charge-transfer complexes TTF can behave as a donor in its neutral form and as an acceptor in its +2 state [90]. Important results have been achieved in intramolecular charge-transfer materials for donor-acceptor molecules or in photoinduced electron transfer when linked to C<sub>60</sub> [89, 91]. Mixed-valence compounds like TTF are the prototypes of molecules able to undergo fast electron transfer through a bridge. Such systems are used to study intramolecular electron-transfer (IET) between redox centers with the aim to understand electron-transfer processes. In terms of supramolecular chemistry, sensors and molecular switches based on TTF-containing rotaxanes and catenanes have been prepared [92]. These properties make TTF an interesting candidate for molecular electronics.

We performed conductance measurements on TTF derivatives with the goal to address chemically the different charge states of the redox molecule and consequently to observe an effect on its conductivity. A nearly tenfold increase in the tunneling current through the redox compound Fe(III)-protoporphyrin was reported when reducing the Fe(III) to Fe(II) [93]. Meanwhile several experiments were carried out to investigate the redox state dependence on the single molecule conductivity [94, 95, 96,

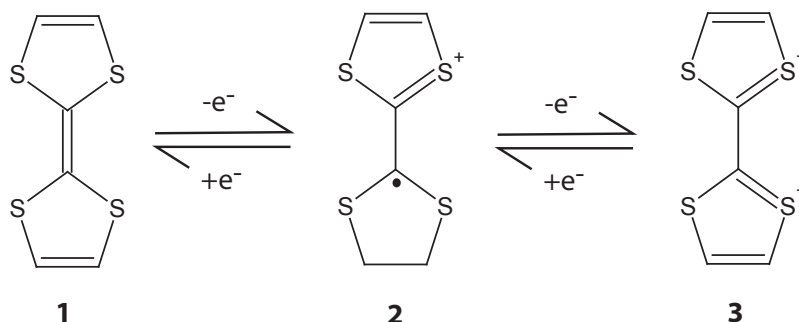


Figure 6.1: Reversible oxidations of TTF.

97].

Acetyl-protected thiol end groups are attached to our TTF compounds providing a chemical bond to the gold surface. In contrast to the single functionalized  $C_{60}$  used in the previous measurement (see Chapter 5) the molecule is now anchored on both sides. This configuration allowed to record stable current-voltage ( $I$ - $V$ ) characteristics in addition to the conductance  $G$  versus distance  $d$ .

## 6.2 Electrochemical gating

An ultimate goal in the field of molecular electronics is to build a single molecule field effect transistor (FET). This challenging aim has already been reached at low temperature where Coulomb blockade and Kondo effect have been observed [3, 4, 16, 98]. An electrochemical carbon nanotube field-effect transistor was demonstrated by Krüger *et al* [17], the liquid-ion gating was by a factor 200 more efficient than a back gating. Recently a large gate effect due to an electrolyte has been observed on a single molecule device [18], where the gate controlled the current over nearly 3 orders of magnitude.

Fig. 6.2 shows a schematics of a single molecule transistor using a conventional back gate (a) and a liquid-ion gate (b). The effect on the transconductance can be maximized if the gate is placed as close as possible to the molecule. Since an electrochemical gate is in intimate contact with the molecule, it has a big advantage compared with a lithographically fabricated gate, which is much further away. The gate voltage falls across the double layers at the electrode-electrolyte interfaces, as indicated in Fig. 6.2(b). As the double layers are only a few ions thick, a field close to  $\sim 1$  V/Å can be reached [18]. The gate capacitance formed by the double layer capacitance can therefore be very large. It is ap-

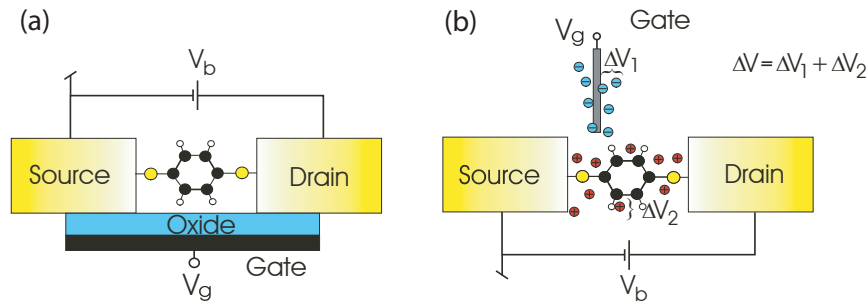


Figure 6.2: Schematics of a single molecule transistor, with a conventional back gate (a) and with a liquid-ion gate (b).

proximately given by  $C_g = 2\pi r\epsilon/\lambda$ , where  $\epsilon$  is the dielectric constant of the medium,  $r$  the molecule radius and  $\lambda$  the Debye length.  $\lambda$  represents the distance between the oppositely charged layers and depends on the concentration  $c$  and the charge of the electrolyte  $z$  ( $\lambda \propto 1/\sqrt{z^2 c}$ ). The gate voltage shifts the energy of the molecular levels. At negative gate voltage, the molecule is surrounded by anions as sketched in Fig. 6.3(a) and the levels of the molecule shift to higher energies. A crossing of the HOMO (highest occupied molecular orbital) with the Fermi level  $E_F$  of the electrode leads then to an increase in the current, due to resonant tunneling [18]. The reverse happens at positive gate voltage, sketched in Fig. 6.3(b). In this case the cations are located around the molecule and the molecular levels shift to lower energies. The LUMO (lowest

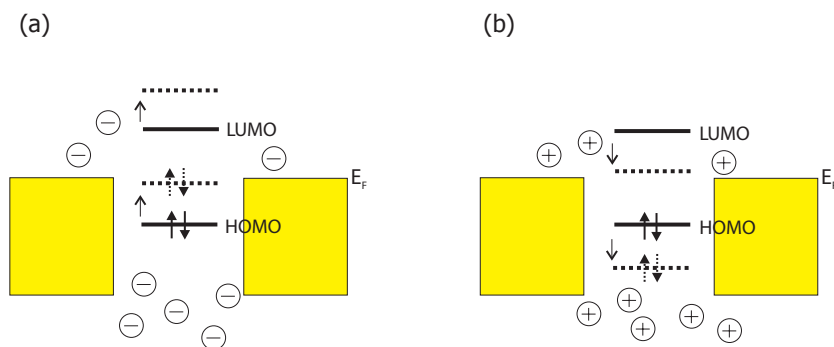


Figure 6.3: Schematics of energy diagram of a molecular transistor with a liquid-ion gate, in (a) at negative gate voltage and in (b) at positive gate voltage. The dashed lines correspond to the gate induced position of the HOMO and the LUMO.

unoccupied molecular orbital) is shifted to the Fermi level  $E_F$  and the current increases.

### 6.3 Experimental part and measurements

We performed measurements on 3 different TTF compounds shown in Fig. 6.4 where **4** has a central TTF unit embedded in the conjugated chain and **5** and **6** are two pyrrolo-annealed TTFs with the TTF on the side of the conjugated chain. Our intention was to investigate whether the conductance of the TTF compound could be modulated by tuning its charge state.

The junction was first characterized via measurements of the conductance  $G$  versus distance  $d$  in the solvent subsequently used for the TTF compound. We performed consecutive open-close cycles with  $G$  ranging between  $0.1 G_0$  and a few  $G_0$  and afterwards in the tunneling regime without fully closing the junction. A 0.3 mM TTF solution was prepared in toluene (for **5** and **6**) whereas compound **4** was dissolved in a (4:1) mixture of toluene/acetonitrile (AN) or dichloromethane ( $\text{CH}_2\text{Cl}_2$ ). In order to improve the assembly of the molecules on the gold surface the acetyl protection group was hydrolyzed with tetrabutylammonium hydroxide (TBAOH) just a few minutes before the experiment (details are described in Appendix B). We could never observe a signal from the

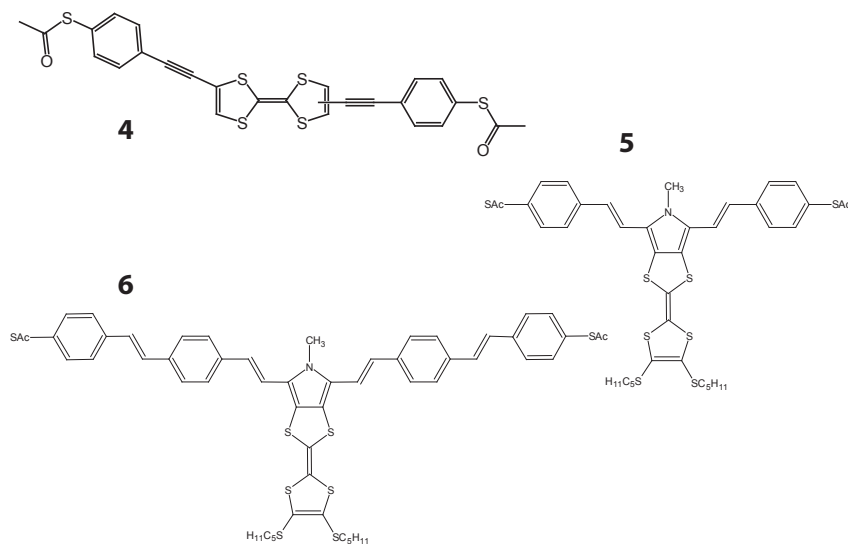


Figure 6.4: The 3 TTF compounds tested in the break junction: **4** with the TTF unit within the conjugated chain whereas in **5** and **6** the pyrrolo-annealed TTF unit is in the side chain of the conjugated wire. **4** was synthesized by N. Martín *et al.*, **5** and **6** by J. Becher *et al.*.

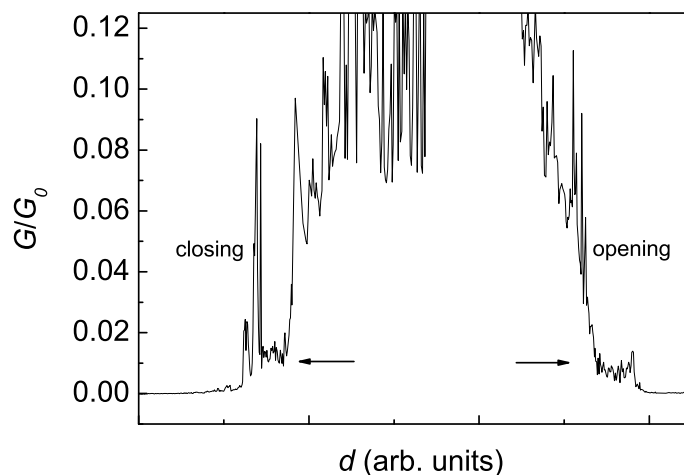


Figure 6.5:  $G$  vs.  $d$  (in arb. units) of TTF compound **4** while decreasing (closing) and increasing (opening) the electrode distance at  $V_b=0.1V$ . Clearly to see are the two plateaus (arrows) indicating that the molecule is attached to both electrodes.

molecule when not removing the protection group although the acetyl group is supposed to cleave by itself on gold [99]. The solution with the molecules was added to the liquid cell while the junction was kept closed. The junction was then opened widely ( $\sim 5$  nm) for a couple of minutes to let the molecules assemble. While approaching the two electrodes we applied a voltage of 0.6-0.8 V to align the polarizable molecules in between the contacts. The current increases first roughly exponentially before it sometimes shows a plateau-like feature. This “lock-in” of the molecule [100] indicates that the molecule is attached to both electrodes. Fig. 6.5 shows an example of two consecutive recorded curves of TTF compound **4** while decreasing the electrode distance (closing) and increasing it again (opening). Both curves reveal a clear plateau (arrows). Various approaches were undertaken in order to study a gate effect: either by modulating the oxidation state of the TTF unit by an oxidation agent and studying its influence on the conductance of the molecule, or by electrochemical gating with an electrolyte. These approaches are described below.

1. One approach consisted of adding an oxidation agent to the TTF solution during the measurement. One could then compare directly the  $I$ - $V$  characteristics of the two different redox states before and after the oxidation. We used a 2 mM  $\text{Fe}(\text{ClO}_4)_3$  solution (in Toluene/AN 4:1) to oxidize the TTF whereupon the  $\text{Fe}^{3+}$  undergoes a reduction to  $\text{Fe}^{2+}$  [101]. An addition of a solution during the measurement is causing turbulences of the liquid in the cell and a mechanical rearrangement of the electrodes can occur. In this

respect the method is rather problematic as it is difficult to estimate if a change in the  $I$ - $V$  curve is generated by an alteration of the oxidation state of the molecule or by a change of the junction conformation.

Iodine ( $I_2$ ) can also be used to oxidize the TTF but it was not compatible with our samples. Briefly after the addition to the liquid cell the junctions broke and the samples were no longer of use.

2. The second approach was also involving  $Fe(ClO_4)_3$  but it was already mixed with the TTF solution before the experiment. This avoids an addition of the oxidation agent and potential turbulences during the measurement. The TTF is supposed to be in the +2 state when starting the experiment. Spectroscopy (UV/VIS) would give information about the exact charge state ([101]).
3. In order to obtain an electrochemical gate effect two types of electrolytes were used. The first electrolyte (0.1 or 0.5 M aqueous  $MgCl_2$ ) was added after assembling the molecules onto the gold electrodes. The second electrolyte (0.1 and 0.5 M tetrabutylammonium hexafluorophosphate ( $Bu_4NPF_6$ ) in toluene/AN 4:1) was either mixed with the molecules before the experiment or added to the liquid cell during the experiment.

## 6.4 Discussion

Due to the stability of the metal-molecule-metal system we were able to record  $I$ - $V$ -characteristics at different positions of the push-rod  $z$ . An example of a measurement of **5** in toluene is shown in Fig. 6.6 where (a) represents the conductance  $G$  versus  $z$ . The movement was stopped at the indicated position Fig. 6.6(a)(arrow) to record the black  $I$ - $V$  curve plotted in Fig. 6.6(b). Afterwards the position was changed by  $25 \mu m$  in  $z$ , corresponding to an approach of the electrodes by  $\sim 1$  nm, and another  $I$ - $V$  taken (red curve). The differential conductance at  $V_{bias}=0$  V for the black curve was  $3.9 \cdot 10^{-3} \mu S$  and for the red curve  $9.8 \cdot 10^{-2} \mu S$ , i.e. the conductance increased by more than one order of magnitude by the position change.

From now on I focus on preliminary measurements of compound **4**. The conductance should be tested in dependence of the gate voltage. Therefore a 0.3 mM solution in Tol:AN (4:1) was prepared, the thiols deprotected and  $Bu_4NPF_6$  added (0.1M). The mixture was inserted in the liquid cell.

$I$ - $V$ -curves for different gate voltages were recorded at 6 different positions in  $z$ . The measurements for the different positions are presented in Appendix C. In order to clarify the presence of a gate-effect we performed the following procedure: The  $dI/dV$  was calculated for the 5 individual

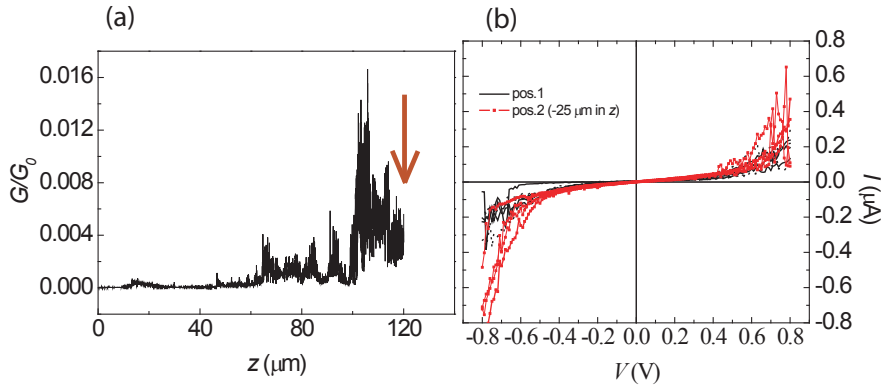


Figure 6.6: (a) Conductance  $G/G_0$  vs.  $z$  (vert. movement) of TTF compound (5) while decreasing (closing) the junction. The motor was stopped at the indicated position (arrow) to record the  $I$ - $V$ -characteristics (black curve) shown in (b). A second curve (red) was taken after moving the  $z$  position by  $-25 \mu\text{m}$  ( $\sim 1 \text{ nm}$  approach of the electrodes) and recording a second  $I$ - $V$  curve.

$I$ - $V$ -curves at  $V_b=0$  (up and down sweeps separately) as well as its standard deviation. This procedure was repeated at different gate voltages ( $V_{gate}=\pm 0.7 \text{ V}$ ,  $\pm 0.6 \text{ V}$ ,  $\pm 0.4 \text{ V}$ ,  $\pm 0.2 \text{ V}$ ,  $0 \text{ V}$ ) and for the 6 push-rod positions. The averaged value of the  $dI/dV$  and the standard deviation (error bar) is plotted in Fig. 6.7(a)/(b) for the 6 different positions (also shown in Appendix C but for each position separately). In between the push-rod position  $z$  was changed. From (1) to (4) the push-rod was moved in  $-z$  direction (corresponding to  $\Delta d_{gap}$ ): from 1 $\rightarrow$ 2 by  $148 \mu\text{m}$  ( $\sim 5 \text{ nm}$ ), from 2 $\rightarrow$ 3 by  $31 \mu\text{m}$  ( $\sim 1 \text{ nm}$ ) and from 3 $\rightarrow$ 4 by  $222 \mu\text{m}$  ( $\sim 7 \text{ nm}$ ). The push-rod was moved upwards again from 4 $\rightarrow$ 5 by  $60 \mu\text{m}$  ( $\sim 2 \text{ nm}$ ) and from 5 $\rightarrow$ 6 downwards again by  $49 \mu\text{m}$  ( $\sim 1.5 \text{ nm}$ ). Notice the large conductance change by opening the gap again from 4 $\rightarrow$ 5 by  $\sim 2 \text{ nm}$ .

To assess the possibility of a gate effect and in order to make a quantitative statement, it is useful to consider the standard deviation of the  $dI/dV$  at each gate voltage. It reveals the fluctuations and drifts of the system during the measurements. While varying the gap distance, the overall conductance changes significantly. The positions (1) and (2) do not obviously reveal a gate effect, the interpolation between the points is almost flat and the averaged conductance values lie inside the error bars. In contrary, position (3) shows an increase in the conductance at  $V_{gate}=-0.4 \text{ V}$  of  $\sim 60\text{-}70\%$  relative to the value at  $V_{gate}=0 \text{ V}$ , but the error bars are large. Also position (4) in Fig. 6.7(b) reveals a certain tendency in the gate dependence despite the error bars are large. The conductance values at  $V_g=\pm 0.7 \text{ V}$  are clearly the lowest compared with the values at

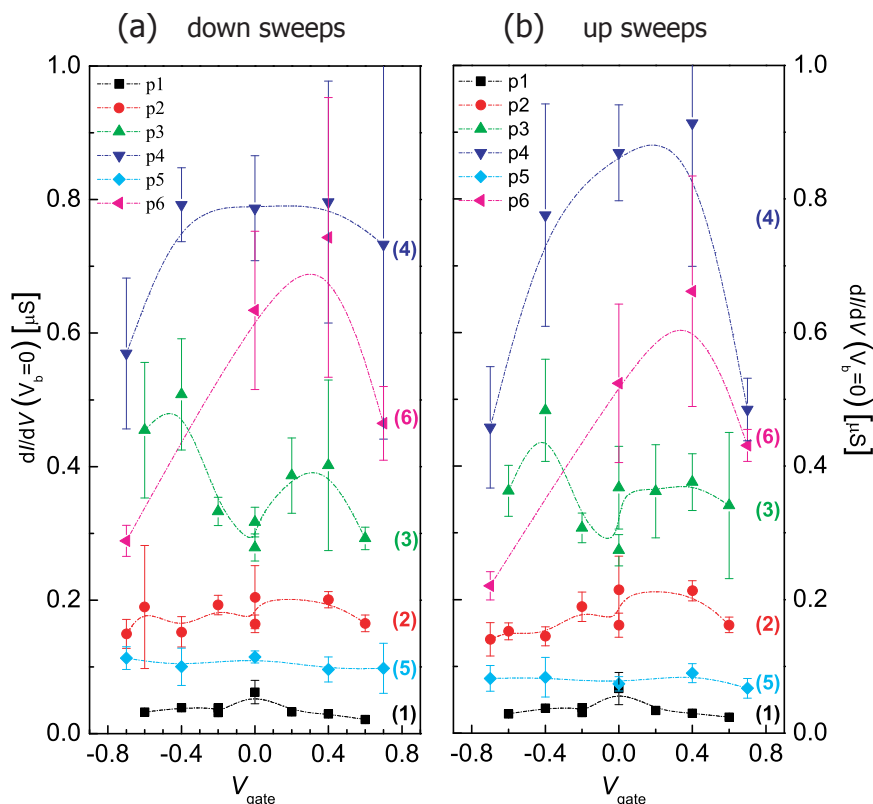


Figure 6.7:  $dI/dV$  ( $V_b=0V$ ) in  $\mu S$  versus gate voltage (PtIr electrode in 0.1 M  $Bu_4NPF_6$  in Tol:AN 4:1) for 6 different positions. The error bar is the standard deviation obtained from the derivative of  $I$ - $V$ -curves.

$\pm 0.4$  V and 0 V. The gate effect at position (4) in Fig. 6.7(a) is due to the large error bar at 0.7 V unclear. Between position (4) and (5) the gap was opened again reflecting the decrease in conductance. Position (6) reveals a similar effect as in position (4): the conductance values at  $V_g = \pm 0.7$  V are clearly lower than the ones at  $V_{gate} = 0$  V and 0.4 V.

The question is whether these partially arising conductance increases are caused by the gate. An important factor in connection with a gate effect is the ratio of the molecular size to the double layer thickness. The TTF compound **4** is about 2.5 nm long. This length defines approximately the separation between the two electrodes. The double layer thickness is  $\sim 1$  nm at each electrode for a 0.1 M electrolyte (type 1:1 in aqueous solution) [102]. Theoretically the two double layers do not overlap in our experiment. But we have to consider, that the calculation for the Debye length  $\lambda$  (double layer) treats the ions as point charges.  $Bu_4NPF_6$  consists of large ions with a smaller charge density than an inorganic electrolyte like e.g.  $LiClO_4$ . In this respect we have to count on  $\lambda > 1$



nm and thus on an overlap of the two double layers. An overlap of the two double layers can strongly affect the gate efficiency [103]. This can be understood in terms of a conventional MOSFET, where the gate oxide thickness needs to be much smaller than the channel length (length of the molecule) for the gate control to be effective [104]. Nevertheless, our results in Fig. 6.7 reveal some variation of the conductance with the gate voltage. However, these variations may have another origin. While moving from one position to the other the configuration of the molecule in the gap can change. This affects the geometry of the molecular junction and thus influences the conductance through the molecule. Slight changes in the position are also possible during the recording of the  $I$ - $V$  characteristics due to the dynamics of the liquid environment. If this occurs while measuring the gate dependency, one has to take into account that the conductance is also influenced by the dynamics of the molecule and not only by the gate voltage.

Beside a polarization of the molecule due to the electrolyte [17] also an oxidation/reduction of the molecule has to be considered. The exact oxidation/reduction potentials of a molecule are obtained by voltammetry. This experiment should be done in order to evaluate the results with the break junction.

To clarify the observed effect shown in Fig. 6.7, more experiments are required. A higher concentration of the electrolyte leads to a thinner double layer ( $\lambda \propto c^{-1/2}$ ). As the potential drop happens across the double layer, measurements at different electrolyte concentrations could give information about the presence of a gate effect. As already mentioned above the size of the ions is not a negligible factor in view of the double layer thickness. Organic ions like  $\text{Bu}_4\text{NPF}_6$  are in this sense not favorable. We therefore carried out another experiment with aqueous  $\text{MgCl}_2$ , but unfortunately we were not able to record  $I$ - $V$  characteristics at different positions.

In addition, more attempts should be made with an oxidation agent to directly access the TTF-unit in the molecule. The two experiments carried out with  $\text{FeClO}_4$  were not convincing. An interesting experiment could be to tune *in situ* the redox couple  $\text{Fe}^{3+} \leftrightarrow \text{Fe}^{2+}$  by the gate voltage. In this way the oxidation state and the conductivity of the TTF is addressed indirectly. Additionally, a reversible switching between the oxidation states would be possible.

An interesting experiment could be to reproduce the reported gate effect on a perylene compound of Xu *et al.* [18]. By using the same conditions we should be able to observe a similar effect. This would be a confirmation that we have an appropriate system for such a type of experiments.

## 6.5 Conclusion

We have performed first conductance measurements of three different TTF compounds. Several attempts to gate the molecule were carried out either with an electrolyte or by use of an oxidation agent.  $I$ - $V$  characteristics at various gate voltages were recorded at different gap distances. The data show some change in the conductance for different gate voltages. Whether this effect is due to the gate is still unclear. Thus more experiments are necessary to prove the existence of a gate effect.

# Bibliography

- [1] M. Madou, *Fundamentals of Microfabrication*, CRS Press LLC, second edition, 2002.
- [2] A. Aviram and M. Ratner, Chem. Phys. Lett. **29**, 277 (1974).
- [3] J. Park et al., Nature **417**, 722 (2002).
- [4] W. Liang, M. Shores, M. Bockrath, J. Long, and H. Park, Nature **417**, 725 (2002).
- [5] J. Chen, M. Reed, A. Rawlett, and J. Tour, Science **286**, 1550 (1999).
- [6] C. Collier et al., Science **285**, 391 (1999).
- [7] M. Reed, C. Zhou, C. Muller, T. Burgin, and J. Tour, Science **278**, 252 (1997).
- [8] D. Klein, P. McEuen, J. B. Katari, R. Roth, and A. Alivisatos, Appl. Phys. Lett. **68**, 2574 (1996).
- [9] S. Boussaad and N. Tao, Appl. Phys. Lett. **80**, 2398 (2002).
- [10] X. Cui et al., Science **294**, 571 (2001).
- [11] C. Joachim and J. Gimzewski, Chem. Phys. Lett. **265**, 353 (1997).
- [12] B. Xu and N. Tao, Science **301**, 1221 (2003).
- [13] C. Kergueris et al., Phys. Rev. B **59**, 12505 (1999).
- [14] R. Smit et al., Nature **419**, 906 (2002).
- [15] J. Reichert, H. Weber, M. Mayor, and H. v.Löhneysen, Appl. Phys. Lett. **82**, 4137 (2003).
- [16] A. Champagne, A. Pasupathy, and D. Ralph, cond-mat **0409134** (2004).
- [17] M. Krüger, M. Buitelaar, T. Nussbaumer, and C. Schönenberger, Appl. Phys. Lett. **78**, 1291 (2001).

- [18] B. Xu, X. Xiao, X. Yang, L. Zang, and N. Tao, *J. Am. Chem. Soc.* **127**, 2386 (2005).
- [19] F. Jäckel, M. Watson, K. Müllen, and J. Rabe, *Phys. Rev. Lett.* **92**, 188303 (2004).
- [20] R. Waser, *Nanoelectronics and Information Technology*, Wiley-VCH GmbH, first edition, 2003.
- [21] N. Zhitenev, A. Erbe, and Z. Bao, *Phys. Rev. Lett.* **92**, 186805 (2004).
- [22] C. Schönenberger, J. Sondag-Huethorst, J. Jorritsma, and L. Fokkink, *Langmuir* **10**, 611 (1994).
- [23] M. Krueger, *Towards Single Molecule Electronics*, PhD thesis, Universität Basel and unpublished, 2000.
- [24] C. Schönenberger et al., *J. Phys. Chem. B* **101**, 5497 (1997).
- [25] J. Gimzewski and R. Möller, *Phys. Rev. B* **36**, 1284 (1987).
- [26] J. Moreland, S. Alexander, M. Cox, R. Sonnenfeld, and P. Hansma, *Appl. Phys. Lett.* **43**, 387 (1993).
- [27] J. Moreland and J. Ekin, *J. Appl. Phys.* **58**, 3888 (1985).
- [28] C. Muller, J. van Ruitenbeek, and L. de Jongh, *Phys. Rev. Lett.* **69**, 140 (1992).
- [29] C. Muller, J. van Ruitenbeek, and L. de Jongh, *Phys. Rev. Lett.* **69**, 140 (1992).
- [30] L. Olesen et al., *Phys. Rev. Lett.* **72**, 2251 (1994).
- [31] J. Krans et al., *Phys. Rev. B* **48**, 14721 (1993).
- [32] N. Agraït, J. Rodrigo, and S. Vieira, *Phys. Rev. B* **47**, 12345 (1993).
- [33] C. Muller, J. Krans, T. Todorov, and M. Reed, *Phys. Rev. B* **53**, 1022 (1996).
- [34] G. Rubio, N. Agraït, and S. Vieira, *Phys. Rev. Lett.* **76**, 2302 (1996).
- [35] E. Scheer, P. Joyez, D. Esteve, C. Urbina, and M. Devoret, *Phys. Rev. Lett.* **78**, 3535 (1997).
- [36] E. Scheer et al., *Nature* **394**, 154 (1998).
- [37] J. Reichert et al., *Phys. Rev. Lett.* **88**, 17 (2002).

- [38] R. Smit et al., *Nature* **419**, 906 (2002).
- [39] D. Dulić et al., *Phys. Rev. Lett.* **91**, 207402 (2003).
- [40] N. Agraït, A. Yeyati, and J. van Ruitenbeek, *Physics Reports* **377**, 81 (2003).
- [41] H. Ohnishi, Y. Kondo, and K. Takayanagi, *Nature* **395**, 780 (1998).
- [42] C. Sirvent, J. Rodrigo, N. Agraït, and S. Vieira, *Physica B* **218**, 238 (1996).
- [43] J. Costa-Krämer, N. García, and H. Olin, *Phys. Rev. B* **55**, 12910 (1997).
- [44] C. Zhou, C. Muller, M. Deshpande, J. Sleight, and M. Reed, *Appl. Phys. Lett.* **67**, 1160 (1995).
- [45] J. Ruitenbeek et al., *Rev. Sci. Instrum.* **67**, 108 (1996).
- [46] W. Young, *Roark's Formulas for Stress and Strain*, Mc Graw-Hill Book Company, New York, 6th edition, 1989.
- [47] S. Vrouwe et al., *Phys. Rev. B* **71**, 035313 (2005).
- [48] O. Kolesnychenko, O. Shklyaresvskii, and H. van Kempen, *Rev. Sci. Instrum.* **70**, 1442 (1999).
- [49] T. Todorov and A. Sutton, *Phys. Rev. Lett.* **70**, 2138 (1993).
- [50] U. Landman, W. Luedtke, B. Salisbury, and R. Whetten, *Phys. Rev. Lett.* **77**, 1362 (1996).
- [51] G. Finbow, R. Lynden-Bell, and I. McDonald, *Molecular Physics* **92**, 705 (1997).
- [52] M. Sørensen, M. Brandbyge, and K. Jacobsen, *Phys. Rev. B* **57**, 3283 (1998).
- [53] C. Untiedt et al., *Phys. Rev. B* **66**, 085418 (2002).
- [54] A. Yanson, G. Bollinger, H. van den Brom, N. Agraït, and J. van Ruitenbeek, *Nature* **395**, 783 (1998).
- [55] T. Böhler, J. Grebing, A. Mayer-Gindner, H. von Löneysen, and E. Scheer, *Nanotechnology* **15**, S465 (2004).
- [56] J. Pethica and A. Sutton, *J. Vac. Sci. Technol. A* **6**, 2490 (1988).
- [57] P. Taylor, J. Nelson, and B. Dodson, *Phys. Rev. B* **44**, 5834 (1991).

- [58] M. Sørensen and K. J. H. Jónsson, *Phys. Rev. Lett.* **77**, 5067 (1996).
- [59] K. Hansen et al., *Appl. Phys. Lett.* **77**, 708 (2000).
- [60] J. Cuevas, A. Yeyati, and A. Martin-Rodero, *Phys. Rev. Lett.* **80**, 1066 (1998).
- [61] W. Schmickler and D. Henderson, *J. Electroanal. Chem.* **290**, 283 (1990).
- [62] J. Sass, J. Gimzewski, W. Weiss, K. Besocke, and D. Lackey, *Condens. Matter* **3**, S121 (1991).
- [63] S. Boussaad et al., *Journal of Chemical Physics* **118**, 8891 (2003).
- [64] S. Lindsay et al., **288**, 25 (1995).
- [65] M. Hugelmann and W. Schindler, *Surface Science* **541**, L643 (2003).
- [66] W. Schmickler, *Chem. Rev.* **96**, 3177 (1996).
- [67] K. Sebastian and G. Doyen, *Journal of Chemical Physics* **99**, 6677 (1993).
- [68] B. Bhushan, J. Israelachvili, and U. Landman, *Nature* **374**, 607 (1995).
- [69] B. Persson and F. Mugele, *J. Phys.:Condens. Matter* **16**, R295 (2004).
- [70] A. Marchenko, S. Lukyanets, and J. Coustry, *Phys. Rev. B* **65**, 045414 (2002).
- [71] H. Kroto, J. Heath, S. O'Brien, R. Curl, and R. Smalley, *Nature* **318**, 162 (1985).
- [72] M. Dresselhaus, G. Dresselhaus, and P. Eklund, *Science of Fullerenes and Carbon Nanotubes*, Academic Press, Inc., first edition, 1996.
- [73] H. Park et al., *Nature* **407**, 57 (2000).
- [74] D. Porath, Y. Levi, M. Tarabiah, and O. Millo, *Phys. Rev. B* **56**, 9829 (1997).
- [75] W. Green et al., *J. Phys. Chem.* **100**, 14892 (1996).
- [76] O. Gunnarsson et al., *Phys. Rev. Lett.* **74**, 1875 (1995).
- [77] X. Shi, B. Caldwell, K. Chen, and C. Mirkin, *J. Am. Chem. Soc.* **116**, 11598 (1994).

- [78] Y. Marcus et al., J. Phys. Chem. B **105**, 2499 (2001).
- [79] S. Datta, Nanotechnology **15**, S433 (2004).
- [80] S. Datta, *Electronic Transport in Mesoscopic Systems*, Cambridge University Press, first edition, 1995.
- [81] L. Echegoyen and L. Echegoyen, Acc. Chem. Res. **31**, 593 (1998).
- [82] A. Maxwell, P. Brühwiler, A. Nilsson, N. Märtensson, and P. Rudolf, Phys. Rev. B **49**, 10717 (1994).
- [83] G. Gensterblum et al., Phys. Rev. Lett. **67**, 2171 (1991).
- [84] H. Wang et al., Surface Science **442**, L1024 (1999).
- [85] X. Lu, M. Grobis, K. Khoo, S. Louie, and M. Crommie, Phys. Rev. B **70**, 115418 (2004).
- [86] C.-T. Tzeng, W.-S. Lo, J.-Y. Yuh, R.-Y. Chu, and K.-D. Tsuei, Phys. Rev. B **61**, 2263 (2000).
- [87] B. Hoogenboom, R. Hesper, L. Tjeng, and G. Sawatzki, Phys. Rev. B **57**, 11939 (1998).
- [88] F. Zahid, M. Paulsson, and S. Datta, *Advanced Semiconductors and Organic Nano-Techniques*, Academic Press, Inc., first edition, 2003.
- [89] M. Bryce, Adv. Mater **11**, 11 (1999).
- [90] P. Ashton et al., J. Am. Chem. Soc. **121**, 3951 (1999).
- [91] N. Gautier et al., Angew. Chem. Int. Ed. **42**, 2765 (2003).
- [92] M. Nielsen, C. Lomholt, and J. Becher, Forma **15**, 233 (2000).
- [93] N. Tao, Phys. Rev. Lett. **76**, 4066 (1996).
- [94] W. Han et al., J. Phys. Chem. B **101**, 10719 (1997).
- [95] W. Haiss et al., J. Am. Chem. Soc. **125**, 15294 (2003).
- [96] E. Tran, M. Rampi, and G. Whitesides, Angew. Chem. Int. Ed. **43**, 3835 (2004).
- [97] F. Chen et al., Nano Letters **5**, 503 (2005).
- [98] S. Kubatkin et al., Nature **425**, 698 (2004).
- [99] J. Tour et al., J. Am. Chem. Soc. **117**, 9529 (1995).
- [100] H. Weber et al., Chemical Physics **281**, 113 (2002).

- [101] A. Credi et al., *New J. Chem.* **10**, 1061 (1998).
- [102] W. Schmickler, *Grundlagen der Elektrochemie*, Vieweg & Sohn, first edition, 1996.
- [103] X. Xiao, B. Xu, and N. Tao, *Nano Letters* **4**, 267 (2004).
- [104] P. Damle, T. Rakshit, M. Paulsson, and S. Datta, *IEEE Transactions on Nanotechnology* **1**, 145 (2002).



## Appendix A

# Experimental details to the $C_{60}$ measurements

In this appendix the raw data of the conductance curves and histograms of one measurement of  $C_{60}$  in DMSO and toluene are shown. The experiments showed that it is critical to use a freshly prepared solution with molecules. We never observed a reproducible signal while using old solution (old means a couple of days old). From the 4 attempts with fresh DMSO solution we observed twice a clear reproducible signal from the molecule. In the other two cases the signal was unclear, some curves revealed peaks and plateaus, but it was not reproducible as in the measurement shown below. When using old solution the signal was always unclear and not reproducible, sometimes there was not even a signal. The same holds for  $C_{60}$  dissolved in toluene. From the two experiments with fresh solutions, we observed once a very stable shape in the curves (see below). The second measurement did not show reproducible curves but a clear peak at  $0.02 G_0$  in the histogram. All the other measurements were rather unclear.

The two sequences of  $C_{60}$  in DMSO and toluene shown below display the development of the peak in the conductance curves and in the histogram with time.

### A.1 Measurements of $C_{60}$ in DMSO

Several sets of consecutive open-close cycles were recorded at a time interval of  $\sim 30$ -40 minutes. Fig. A.1 shows representative conductance curves while opening and closing the junction. The curves are plotted versus vertical displacement  $z$  of the push-rod. The measurement sets are recorded at different times. The corresponding histograms of the measured sets (30 curves) are plotted in figure A.2. Each histogram is built from the 30 conductance traces of one set (bin width  $2 \times 10^{-4} G_0$ ) and normalized by the total number of points.

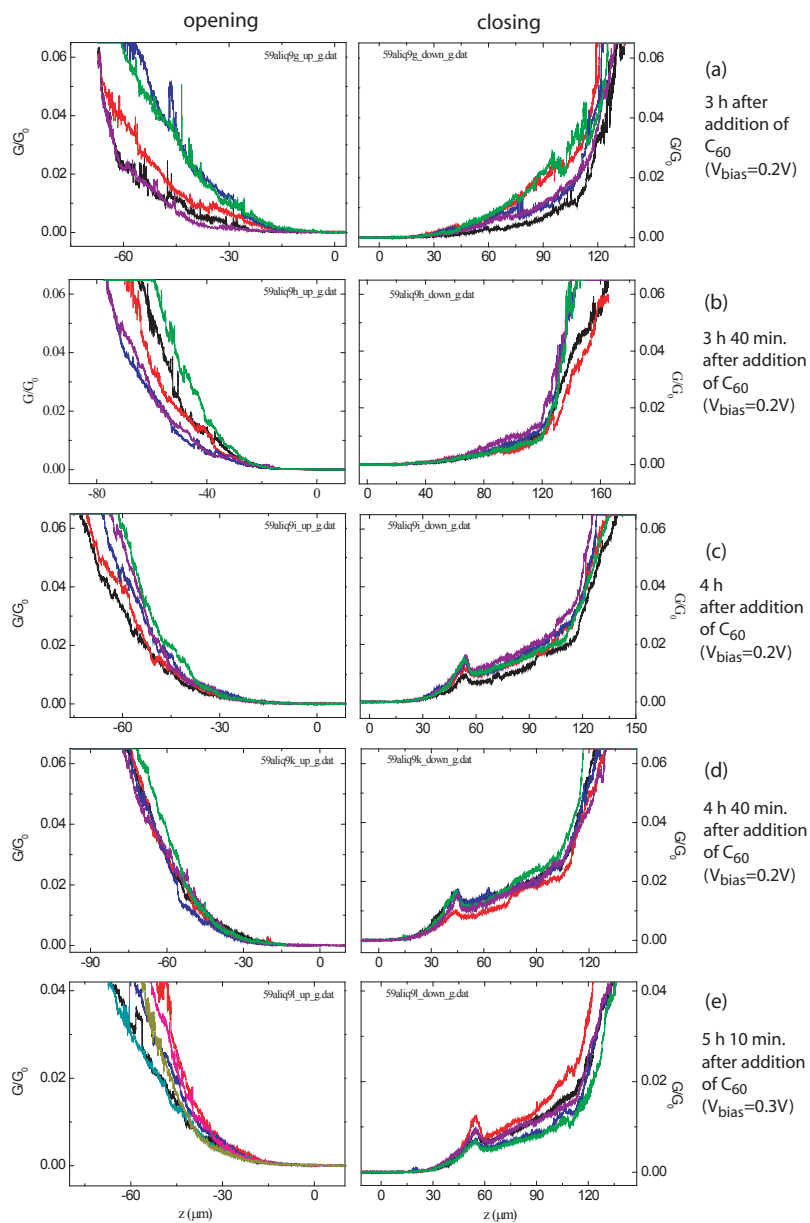


Figure A.1:  $C_{60}$  in DMSO: Conductance  $G/G_0$  versus  $z$  of opening and closing curves after different waiting times.

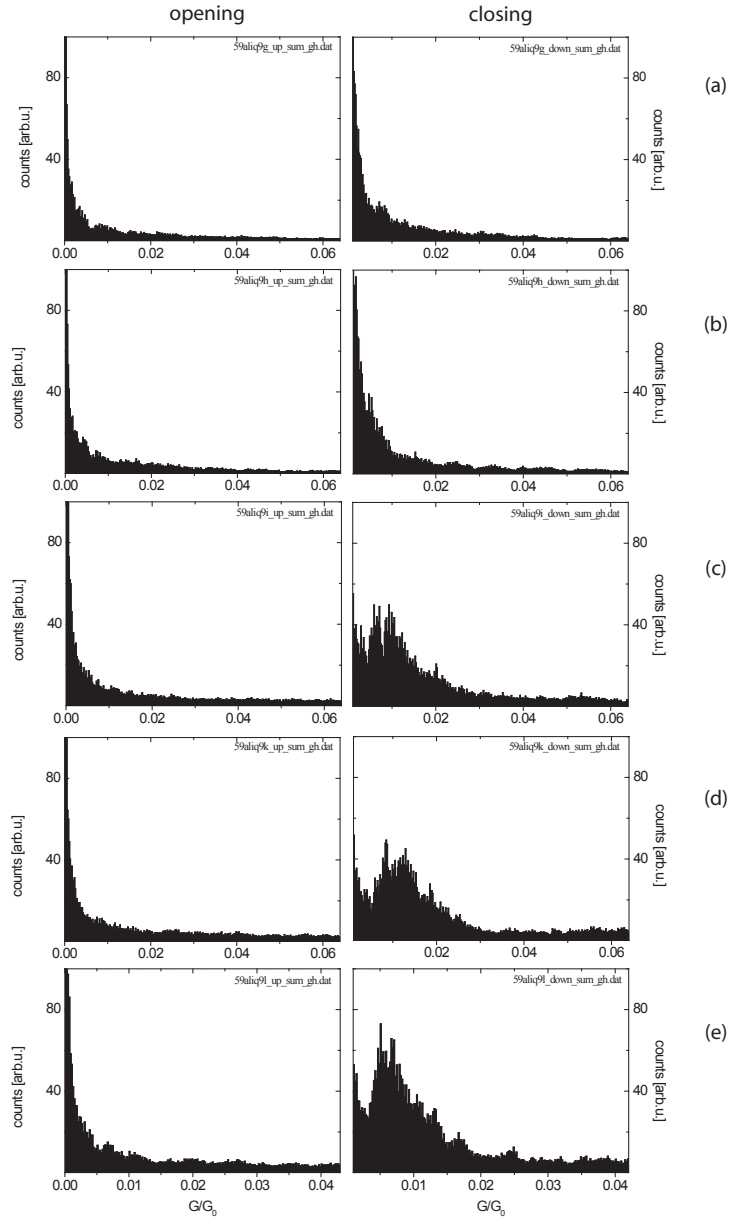


Figure A.2:  $C_{60}$  in DMSO: Conductance histograms in  $G/G_0$  built from 30 conductance traces as shown in Fig. A.1.

## A.2 Measurements of $C_{60}$ in toluene

Several sets of consecutive open-close cycles were recorded at with a time interval of  $\sim 30$ -40 minutes. Fig. A.3 shows representative conductance curves of recorded sets. Between measurements (c) and (d), the junction was flushed with toluene causing the peak in the conductance curve to disappear. After adding  $C_{60}$  in toluene again a signal reemerged (e) but not with the same clear and reproducible shape as in (c). The corresponding histograms are plotted in Fig. A.4. Each histogram is built from the 10 conductance traces of one set (bin width  $2 \times 10^{-4} G_0$ ) and normalized by the total number of points.

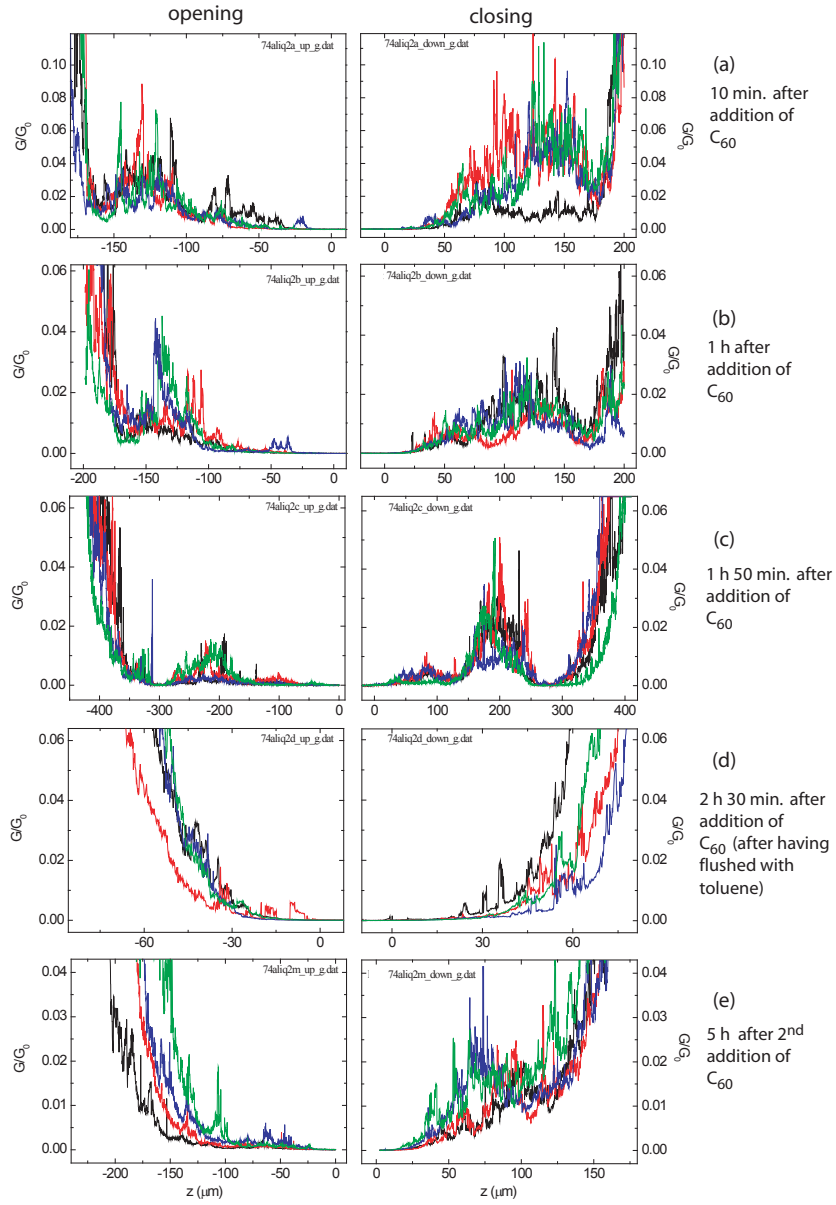


Figure A.3:  $C_{60}$  in toluene: Conductance  $G/G_0$  versus  $z$  of opening and closing curves after different waiting times. Between (c) and (d) the junction was flushed with toluene.

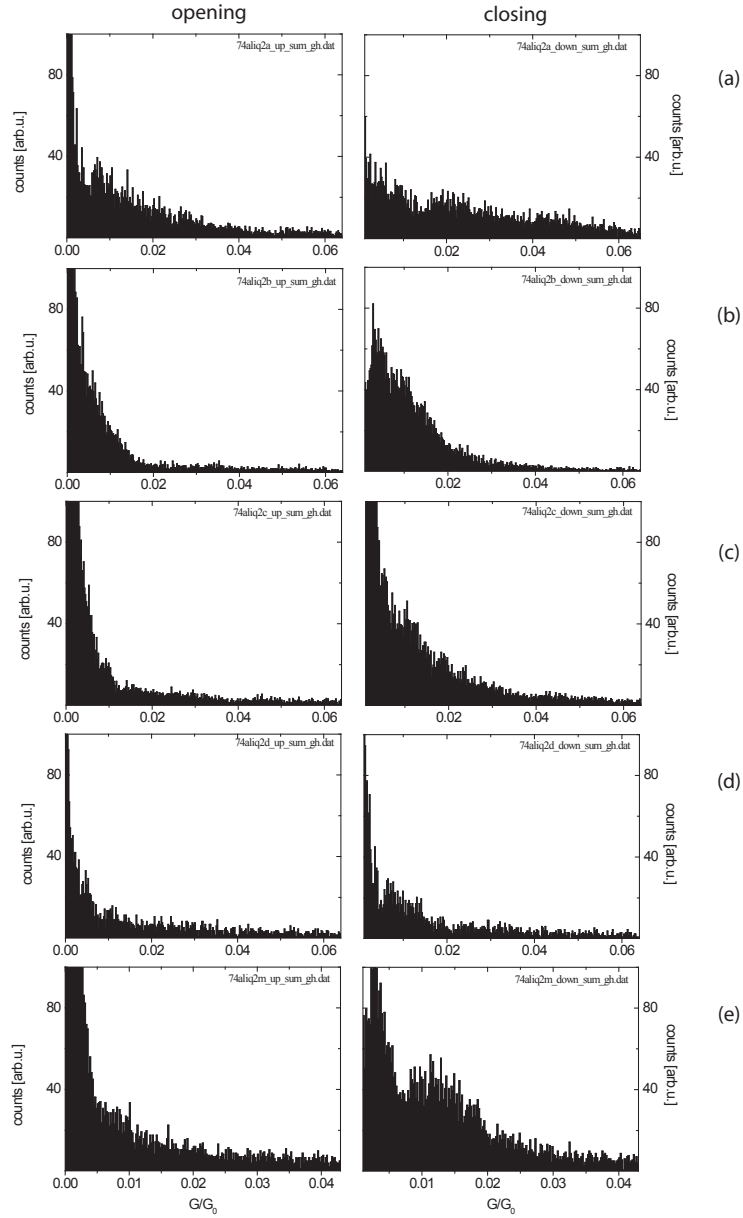


Figure A.4:  $C_{60}$  in toluene: Conductance histograms in  $G/G_0$  built from 10 conductance traces as shown in Fig. A.1.

## Appendix B

# Experimental details to the chemistry of the thiols

The hydrolysis of the acetyl protection group of the thiols was carried out with 0.8 M tetrabutylammonium hydroxide (TBAOH) in methanol (Fluka 86882). TBAOH was added to the thiols in excess in order to have a complete deprotection, i.e. to 1  $\mu\text{mol}$  of TTF we added 5.7  $\mu\text{mol}$  of TBAOH. As the transfer of such small volumes can lead to large errors, a dilution of TBAOH was used: 100  $\mu\text{l}$  TBAOH was diluted in 600  $\mu\text{l}$  Tol/AN (4:1) (or in  $\text{CH}_2\text{Cl}_2$  if this was the solvent of choice for the molecules). 100  $\mu\text{l}$  (contains 5.7  $\mu\text{mol}$  TBAOH) from this mixture was added to the TTF solution. The solution was stirred for a few minutes and immediately transferred in the liquid cell.





## Appendix C

# Additional data to the TTF measurements

In this appendix the raw data and additional data of the analysis to the measurement of the TTF compound **4** are shown. The  $I$ - $V$ -characteristics are presented for the different gate voltages. Each curve in Fig. C.1 and Fig. C.2 is the average of the 5 curves, for “up” sweeps and “down” sweeps, separately. The  $I$ - $V$ -curves were recorded at 6 different positions of the vertical displacement  $z$  at different gate voltages ( $\text{Bu}_4\text{NPF}_6$  in toluene/AN (4:1) with a PtIr wire).

Fig. C.3 and Fig. C.4 present the  $dI/dV$  at  $V_{bias}=0V$  versus gate voltage recorded at 6 different  $z$  positions. They are plotted for each position separately.

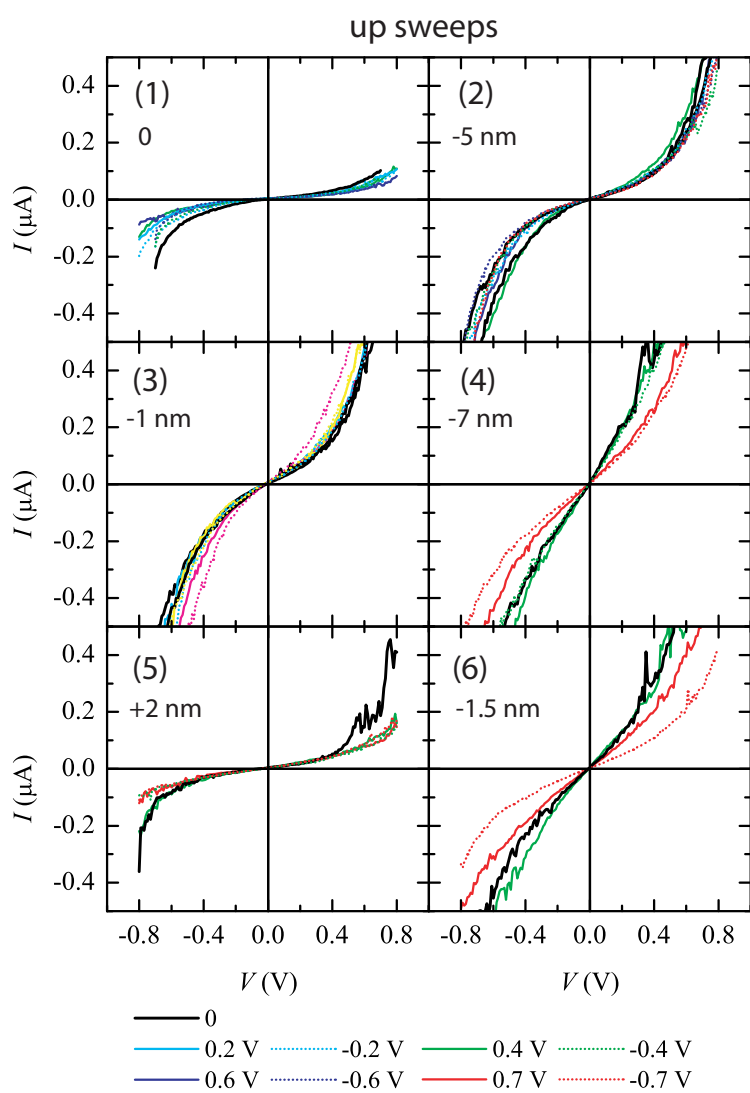


Figure C.1: TTF compound 4 in toluene/AN (4:1) with  $\text{Bu}_4\text{NPF}_6$ .  $I$ - $V$ -characteristics (up sweeps) at 6 different vertical positions  $z$  and different gate voltages (indicated in the legend).

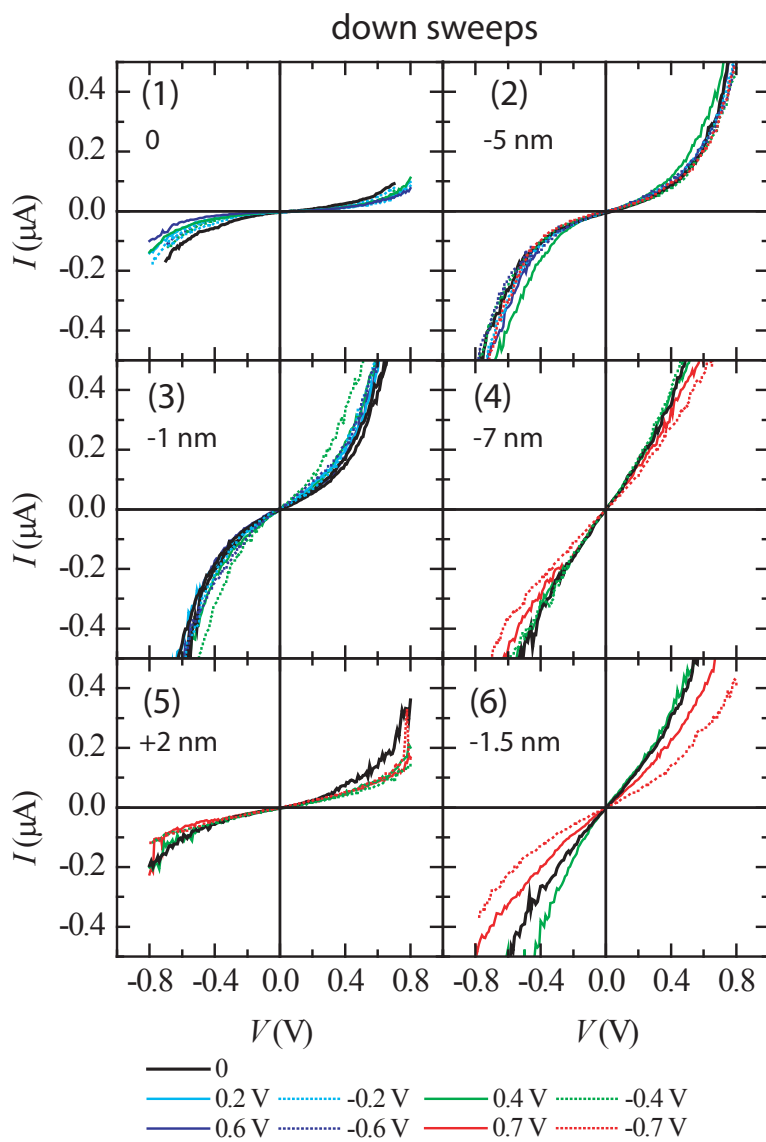


Figure C.2: TTF compound 4 in toluene/AN (4:1) with  $\text{Bu}_4\text{NPF}_6$ .  $I$ - $V$ -characteristics (down sweeps) at 6 different vertical positions  $z$  and different gate voltages (indicated in the legend).

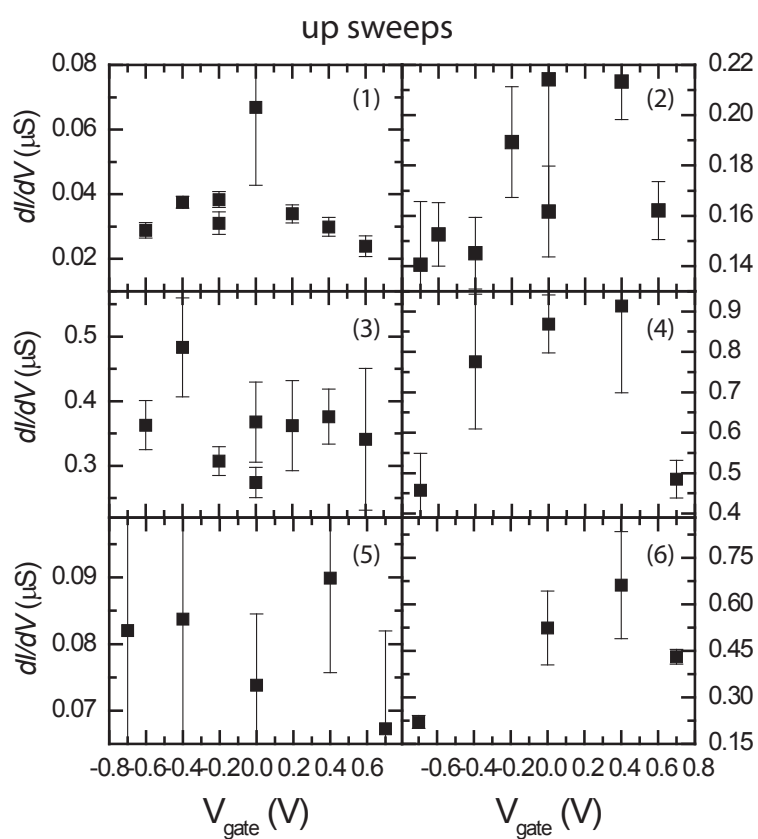


Figure C.3: TTF compound 4 in toluene/AN (4:1) with  $\text{Bu}_4\text{NPF}_6$ .  $dI/dV$  and the standard deviation versus  $V_{\text{gate}}$  at 6 different vertical positions  $z$ , obtained from the derivative of the “up” swept  $I$ - $V$ -curves.

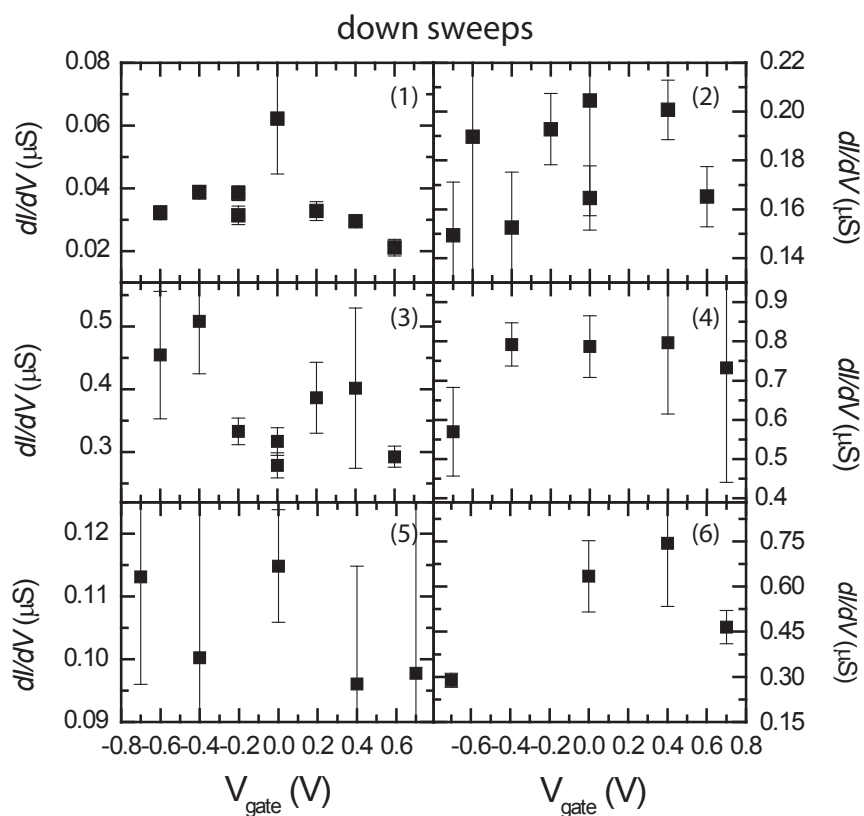


Figure C.4: TTF compound **4** in toluene/AN (4:1) with  $Bu_4NPF_6$ .  $dI/dV$  and the standard deviation versus  $V_{gate}$  at 6 different vertical positions  $z$ , obtained from the derivative of the “down” swept  $I$ - $V$ -curves.



# Publication list

- *Rotationally resolved  $A^3\Sigma_u^- X^3\Sigma_g^-$  electronic transition of  $NC_5N$* , H. Linnartz, O. Vaizert, P. Cias, L. Grüter and J. P. Maier, Chem. Phys. Lett. **345**, 89 (2001).
- *Conductance of atomic contacts in liquid environment*, L. Grüter, M.T. González, R. Hueber, M. Calame and C. Schönberger, cond-mat/0410666, accepted for publication at Small.
- *Resonant tunneling through a  $C_{60}$  molecular junction in liquid environment*, L. Grüter, F. Cheng, T. T. Heikkilä, M. T. González, F. Diederich, C. Schönberger and M. Calame, Nanotechnology **16**, 2143 (2005).





# Talks

- *Break junction in liquid*, NCCR MiniWorkshop on Molecular Electronics, ETHZ, Feb 17, 2004
- *Break junctions for molecular electronics*, 5th International Wilhelm and Else Heraeus Summerschool on “Molecules: Building Blocks for Future Nanoelectronics” at Wittenberg, Germany, Aug. 2-13, 2004
- *Break Junction for Molecular Electronics*, NCCR Meeting on Molecular Electronics, Uni Basel, Sept. 7, 2004



# Posters contributions

- *The link from macro to nano in the framework of single molecule conductivity measurements*, L. Grüter *et al.*, IX International Summer School Nicolas Cabrera on Molecular Electronics, Spain, Sept 15-20, 2002
- *The link from macro to nano in the framework of single molecule conductivity measurements*, L. Grüter *et al.*, Twannberg Workshop on Nanoscience (Switzerland), Sept. 30-Oct. 4, 2002
- *Break Junctions and Nanogaps for Molecular Electronics*, SFB 513 Workshop 2003 and Krupp-Symposium at Konstanz (Germany), July 6-9, 2003
- *Break Junctions and Nanogaps for Molecular Electronics*, Poster at the Swiss/US Nanoforum Basel, Switzerland, Oct 13-14, 2003



# Curriculum Vitae

Lucia Grüter

15. 3. 1971	Geboren in Luzern
1978-1988	Besuch der Primar- und Sekundarschule in Ruswil und Wolhusen
1988-1991	Lehre als medizinisch technische Laborantin mit Schwerpunkt Pathologie, Kantonsspital Luzern
1991-1993	Laborantin im Bereich Mykologie, Institut für Medizinische Mikrobiologie der Universität Zürich
1993	4 monatiger Sprachaufenthalt in Paris (Sorbonne)
1994-1997	Maturitätskurs für Erwachsene (MKE Luzern)
1994-1995	Laborantin am Institut für Pathologie, Kantonsspital Luzern
1995-1997	Laborantin im Bereich Serologie, Labor Dr. Günthert, Luzern
1997-2001	Chemiestudium an der Universität Basel mit Wahlfach Physik
2000	Zweimonatiges Praktikum an der National Synchrotron Light Source am Brookhaven National Laboratory, USA
2001	Diplomarbeit zum Thema: "Laserspektroskopie von metastabilen Kohlenstoffketten" bei Prof. Dr. J.P. Maier, Institut für Physikalische Chemie, Universität Basel
2001	Diplom in Chemie
2001	Zweimonatiger Sprachaufenthalt in Melbourne (Australien)
2002	Beginn der vorliegenden Dissertation zum Thema "Mechanically Controllable Break Junction in Liquid Environment"
2002-2005	Assistenz im Anfängerpraktikum sowie zu den Vorlesungen "Physik I, II und IV".

**Folgenden Dozentinnen und Dozenten verdanke ich meine wissenschaftliche Ausbildung:**

E. Constable, B. Giese, M. Jungen, P. Hauser, C. Housecroft, H. Huber, T. Kaden, J.-P. Maier, W. Meier, M. Neuburger-Zehnder, M. Ohme, A. Pfaltz, C. Schönenberger, U. Séequin, H. Siegel, P. Stratzewski, L. Tauscher, D. Trautmann, H.-J. Wirz, W.-D. Woggon, A. Zuberbühler.

# Danksagung

An dieser Stelle möchte ich mich bei allen bedanken, die mich während meiner Doktorarbeit unterstützt haben. Mein ganz besonderer Dank geht an Prof. Dr. Christian Schönenberger für die Anleitung dieser wissenschaftlichen Arbeit und die vielen lehrreichen Diskussionen. Mit seinem Enthusiasmus konnte er mich immer wieder anstecken, wenn die Arbeit gerade nicht nach Wunsch lief. Prof. Elke Scheer von der Universität Konstanz und Prof. Marcel Mayor von der Universität Basel danke ich sehr für die Übernahme des Korreferats. Bei Christian Urbina möchte ich mich bedanken für die Einladung zu einem Besuch in Saclay. Dort habe ich die Probenherstellung für Break Junction Experimente erlernt. Ein grosses Dankeschön geht an Michel Calame, der mir im Labor immer tatkräftig zur Seite stand und sich immer Zeit nahm für interessante Diskussionen. In diesem Zusammenhang möchte ich mich auch bei Teresa González und Roman Hueber bedanken für die gute Zusammenarbeit und die Unterstützung. Sehr wertvoll für mich waren auch die Diskussionen mit Tero Heikkilä betreffend den  $C_{60}$  Messungen, bei denen ich Einiges über "Resonant Tunneling" gelernt habe.

Im Weiteren möchte ich mich bei Matthias Gräber und Christian Hoffmann bedanken für die amüsanten Slapstick-Einlagen und die vielen interessanten Diskussionen, die weit übers Thema Physik herausgingen. Ausserdem danke die allen Mitgliedern der Gruppe Schönenberger für die gegenseitige Unterstützung: Bakir Babic, Laetitia Bernard, Erasmus Bieri, Mark Buitelaar, Jürg Furer, Matthias Gräber, Gunnar Gunnarsson, Christian Hoffmann, Soufiane Ifadir, Dino Keller, Jianhui Liao, Zeng Ming, Thomas Nussbaumer, Stefan Oberholzer, Sangeeta Sahoo. Ein grosses Dankeschön geht auch an die Mitarbeiter der mechanischen Werkstatt. Ganz besonders geschätzt habe ich die ausserordentliche Hilfsbereitschaft von Herrn Roth, Heinz Breitenstein und Silvester Jakob, die bei Bedarf immer sofort zur Stelle waren. Äusserst wertvoll war auch die Unterstützung von Michael Steinacher und allen anderen Mitarbeitern der Elektronik-Werkstatt.

Diese Arbeit wurde vom National Center of Competence and Research (NCCR) finanziert. Der Druck der Dissertation wurde mit einem Beitrag des Werenfels-Fonds der Freien Akademischen Gesellschaft (FAG) unterstützt.